PROCEEDINGS OF SPIE

SPIEDigitalLibrary.org/conference-proceedings-of-spie

Pre-flight integration and characterization of the SPIDER balloon-borne telescope

A. S. Rahlin, P. A. R. Ade, M. Amiri, S. J. Benton, J. J. Bock, et al.

SPIE.

Pre-flight integration and characterization of the SPIDER balloon-borne telescope

A. S. Rahlin[†,a], P. A. R. Ade[b], M. Amiri[c], S. J. Benton[d], J. J. Bock[e,f], J. R. Bond[g,h], S. A. Bryan[i], H. C. Chiang[j], C. R. Contaldi[k], B. P. Crill[e,f], O. Doré[e,f], M. Farhang[d,g], J. P. Filippini[e], L. M. Fissel[d,l], A. A. Fraisse[a], A. E. Gambrel[a], N. N. Gandilo[m], S. Golwala[e], J. E. Gudmundsson[a], M. Halpern[c,h], M. F. Hasselfield[n,c], G. Hilton[o], W. A. Holmes[f], V. V. Hristov[e], K. D. Irwin[p,q,o], W. C. Jones[a], Z. D. Kermish[a], C. L. Kuo[p,q], C. J. MacTavish[r], P. V. Mason[e], K. Megerian[f], L. Moncelsi[e], T. A. Morford[e], J. M. Nagy[i], C. B. Netterfield[m,d,h], R. O'Brient[e,f], C. Reintsema[o], J. E. Ruhl[i], M. C. Runyan[f], J. A. Shariff[m], J. D. Soler[s,m], A. Trangsrud[f], C. Tucker[b], R. S. Tucker[e], A. D. Turner[f], A. C. Weber[f], D. V. Wiebe[c], and E. Y. Young[a]

[a]Department of Physics, Princeton University, Princeton, NJ, USA;
[b]School of Physics and Astronomy, Cardiff University, Cardiff, UK;
[c]Department of Physics and Astronomy, University of British Columbia, Vancouver, BC, Canada;
[d]Department of Physics, University of Toronto, Toronto, ON, Canada;
[e]Division of Physics, Mathematics and Astronomy, California Institute of Technology, Pasadena, CA, USA;
[f]Jet Propulsion Laboratory, Pasadena, CA, USA;
[g]Canadian Institute for Theoretical Astrophysics, University of Toronto, Toronto, ON, Canada;
[h]Canadian Institute for Advanced Research, Toronto, ON, Canada;
[i]Department of Physics, Case Western Reserve University, Cleveland, OH, USA;
[j]School of Mathematics, Statistics and Computer Science, University of KwaZulu-Natal, Durban, South Africa;
[k]Theoretical Physics, Blackett Laboratory, Imperial College, London, UK;
[l]CIERA, Northwestern University, Evanston, IL, US;
[m]Department of Astronomy and Astrophysics, University of Toronto, Toronto, ON, Canada;
[n]Department of Astrophysical Sciences, Princeton, NJ, USA;
[o]National Institute of Standards and Technology, Boulder, CO, USA;
[p]Department of Physics, Stanford University, Stanford, CA, USA;
[q]Kavli Institute for Particle Astrophysics and Cosmology, SLAC National Accelerator Laboratory, Menlo Park, CA, USA;
[r]Kavli Institute for Cosmology, University of Cambridge, Cambridge, UK;
[s]Institut d'Astrophysique Spatiale, Orsay, France

ABSTRACT

We present the results of integration and characterization of the SPIDER instrument after the 2013 pre-flight campaign. SPIDER is a balloon-borne polarimeter designed to probe the primordial gravitational wave signal in the degree-scale B-mode polarization of the cosmic microwave background. With six independent telescopes housing over 2000 detectors in the 94 GHz and 150 GHz frequency bands, SPIDER will map 7.5% of the sky with a depth of 11 to 14 μK·arcmin at each frequency, which is a factor of $\sim$5 improvement over *Planck*. We discuss the integration of the pointing, cryogenic, electronics, and power sub-systems, as well as pre-flight characterization

---

[†]Corresponding author. Email: arahlin@princeton.edu.

of the detectors and optical systems. SPIDER is well prepared for a December 2014 flight from Antarctica, and is expected to be limited by astrophysical foreground emission, and not instrumental sensitivity, over the survey region.

Keywords: SPIDER, cosmic microwave background, polarization, inflation, transition-edge sensor, scientific ballooning, millimeter wave instrumentation, cosmology.

1. INTRODUCTION

The past twenty years have seen the field of cosmology expand at a rapid pace, from the first hints of anisotropies in the Cosmic Microwave Background (CMB) detected by COBE,[1] to precision tests of the Standard Cosmological Model by the latest generation of CMB experiments[2–8] and complementary datasets, such as late-time measurements of the scale of baryon-acoustic oscillations,[9] and direct measurements of the Hubble parameter.[10]

The CMB traces the distribution of matter in the photon-baryon fluid of the early universe, and anisotropies in this distribution are the seeds of structure formation that evolve into the galaxies and clusters that we observe today. The same density perturbations that generate the temperature anisotropies also generate a polarization pattern on the sky by means of Thomson scattering within the local quadrupole moments of the radiation distribution. The temperature anisotropies and associated intrinsic polarization are well described by the six-parameter ΛCDM model, in which dark energy (Λ) and cold dark matter (CDM) dominate the energy budget of the universe. This polarization pattern, also called the E-mode, has a distinct curl-free geometric signature that has been precisely measured[2, 7, 11, 12] and is consistent with that expected from ΛCDM. In fact, the most recent data from the *Planck* satellite appear remarkably insensitive to any extension beyond the simple six-parameter case,[4] such as extra relativistic degrees of freedom, running of the scalar spectral index, or spatial curvature.

The next generation of cosmological experiments aim to push the limits of the ΛCDM paradigm. The leading hypothesis for the mechanism that shaped the nearly flat, homogeneous and isotropic universe that we observe is a period of super-luminal inflation, occurring in the first instants after the Big Bang. While these characteristics, together with the nearly scale-invariant spectrum of primordial fluctuations and the lack of any detectable departures from Gaussianity provide substantial support for the inflationary paradigm, the detection of an appreciable level of tensor fluctuations via a gravitationally sourced quadrupole would represent significant evidence in favor of the most simple of the inflationary theories. The simplest forms of inflationary models, typically driven by a single scalar field or effective field, predict a curl or B-mode polarization in the CMB at degree angular scales, due to tensor fluctuations induced by early universe gravitational waves.[13] The B-mode amplitude scales with the tensor-to-scalar ratio r, and is expected to peak at degree angular scales with an amplitude 6-7 orders of magnitude fainter than the temperature anisotropy signal. Other hypotheses, such as the ekpyrotic scenario,[14] do not easily admit tensor fluctuations at detectable levels, so a detection of a B-mode signal at large angular scales would favor inflationary models. Alternatively, a stringent limit of $r < 0.01$ would significantly restrict the allowed range of the inflationary scalar field. The strongest limit on r to date is $r < 0.11$ (95% CL), which comes from the *Planck*, ACT and SPT temperature power spectra in conjunction with WMAP 9-year polarization data.[15] Due to the dominant cosmic variance contribution to the limit from temperature data, stronger constraints on r must come from polarized CMB data, where the tensor contribution is more significant.

The strongest limit from the B-mode spectrum alone is about six times greater than the temperature limit at $r < 0.65$ (95% CL), from the BICEP1 3-year analysis.[16] Most recently, the BICEP2 team has claimed a detection of a cosmological B-mode signal corresponding to a tensor-to-scalar ratio greater than the limit from large scale temperature anisotropies.[2] At the time of this writing, there is some evidence that a significant foreground contribution may be bright enough to account for much, if not all, of this signal.[17, 18] The BICEP2 data represent a massive improvement over the state of the art in sensitivity to diffuse polarization. Any experiment aiming to establish a primordial origin for observed B-mode power must (1) confirm that the signal's electromagnetic spectrum is distinct from that of any foregrounds, which requires at least three frequencies for effective separation; (2) confirm that the angular power spectrum is consistent with a cosmological signal; and (3) confirm that the signal is statistically isotropic. *No single experiment to date, including* SPIDER*, has the*
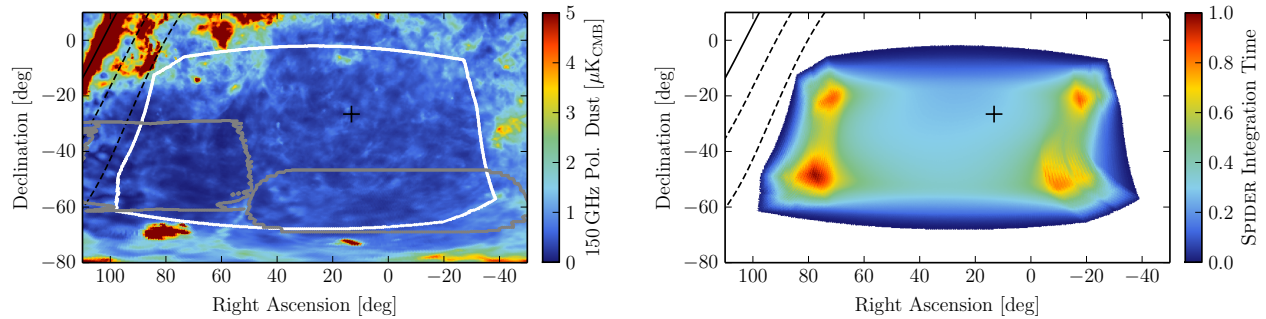
Figure 1. (*left*) Amplitude $P = (Q^2 + U^2)^{1/2}$ of polarized dust at 150 GHz in the southern sky, estimated using the BSS model for dust in the Galactic magnetic field.[19, 20] Galactic latitudes $b = 0°$ (solid), $b = -10°, -20°$ (dashed), and the southern Galactic pole (+) are also shown, along with coverage outlines for SPIDER (white), BOOMERanG (gray, left) and BICEP1/2 (gray, right). (*right*) Distribution of integration time on the sky for a single SPIDER focal plane observing for 24 sidereal hours.

power to definitively address all of these issues. However, as this paper will demonstrate, SPIDER is well-poised to make progress on each of these fronts.

Section 2 discusses SPIDER's science goals and expected sensitivity on the sky. Section 3 provides an overview of the payload systems and proposed flight strategy. Sections 4 and 5 cover the cryogenic and detector performance. Section 6 discusses key aspects of the instrument integration campaign.

2. SCIENCE GOALS

SPIDER is a balloon-borne polarized telescope designed to study the microwave sky at degree angular scales.[20, 21] We plan to observe the southern sky at frequencies of 94 and 150 GHz with an inaugural flight from McMurdo Station, Antarctica in December 2014. We prepared and deployed the completed system for a December 2013 flight, including a successful integration campaign at NASA's Columbia Scientific Balloon Facility (CSBF) in Palestine, TX. However, the U.S. government shutdown resulted in the cancellation of all flights scheduled for that season. In the intervening time, we have been able to perform further characterization and testing of the fully integrated instrument. Table 1 shows a summary of the expected noise performance and map depth after a 16 day flight with an 85% duty cycle over 7.5% of the sky.

The first flight will contain six fully populated receivers, three at each of 94 and 150 GHz, with each containing 144 and 256 pairs of orthogonal polarization-sensitive bolometers, respectively. Each receiver can be independently aligned at various angles with respect to the scan direction, allowing simultaneous observation of both Q and U Stokes parameters. Moreover, an independently controlled stepped half-wave plate (HWP) on each receiver allows modulation of the sky signal to further improve angular coverage, and more importantly, mitigate systematic effects that can create a false polarization signal. The scan strategy, discussed in more detail in Section 3.5, covers the entire observing region once daily. This significant level of redundancy and modularity in the instrument allows for many subdivisions of the data into comparable halves for exhaustive consistency tests.

By launching off the Antarctic coast, SPIDER will have access to a relatively large patch of sky over which to concentrate integration time, as shown in Figure 1. The scan pattern allows for observation of 15% of the

Table 1. Expected instrument parameters for SPIDER's first flight in December 2014, as measured in the lab. Listed are the telescope center frequencies and corresponding bandpass, beam FWHM, total number of light-sensitive detectors, detector yield, and per-detector and total sensitivities. Noise-equivalent temperatures (NETs) are estimated from data acquired under flight-like loading conditions. The map depth assumes an effective sky area of 7.5% covered over a 16 day flight with an 85% duty cycle.

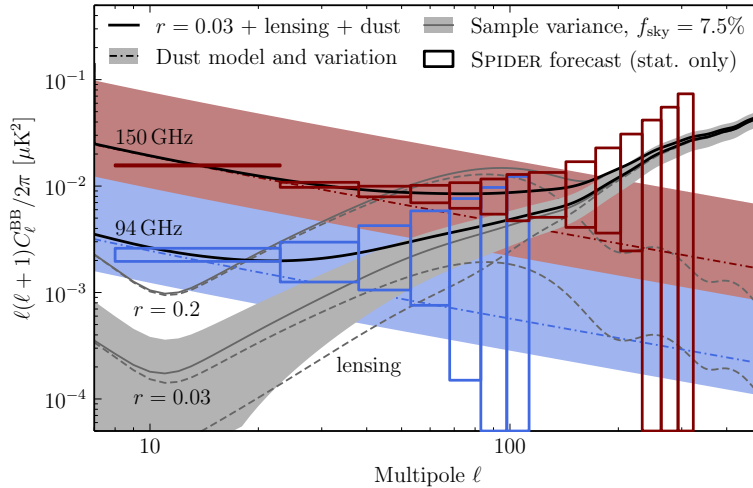| Frequency [GHz]	Bandpass [%]	FWHM [arcmin]	N_{det}	Yield [%]	$\mathrm{NET_{det}}$ [$\mu K\sqrt{s}$]	$\mathrm{NET_{tot}}$ [$\mu K\sqrt{s}$]	Depth [$\mu K \cdot$arcmin]
94	24%	42	864	83%	124	4.6	13.8
150	24%	30	1536	85%	140	3.8	11.2

Figure 2. Forecast for the December 2014 SPIDER flight, based on lab measurements of representative pixels on each focal plane, and detailed in Table 1. The expected statistical sensitivity per bin is shown independently for the 150 GHz (red) and 94 GHz (blue) instruments, overlaid on a dust + lensing + $r = 0.03$ angular power spectrum. The nominal dust amplitude at each frequency (dash-dotted line) is that expected over the SPIDER region based on the BSS model of polarized dust emission,[19, 20] while the surrounding shaded band illustrates the current uncertainty on the dust amplitude in the southern Galactic hemisphere; recent data[18, 24] suggest that dust temperatures may be as much as a factor of two higher than modeled here (corresponding to a factor of four in power). The cosmological sample variance on an $r = 0.03$ + lensing B-mode signal observed over 7.5% of the sky is shown in the gray band. An $r = 0.2$ + lensing spectrum is also shown for reference.

sky while maximizing polarization angle coverage within each pixel; weighting by integration time to maximize signal-to-noise gives an effective sky fraction of 7.5%. This large coverage area reduces the contribution of sample variance at the largest scales and permits high fidelity reconstruction of the shape of the angular power spectrum over many uncorrelated bins at the scales of interest ($10 < \ell < 100$). Moreover, a large observing area gives freedom in selecting independent subregions of the map to test for isotropy of the B-mode signal, and also to enable cross-correlation with other instruments observing within the same regions of the sky, such as ACTpol,[7] SPTpol,[22] BICEP2/Keck,[2] and *Planck*.[23] SPIDER plans to cover the majority of the clean sky available from the southern hemisphere.

By observing at multiple frequencies with similar signal-to-noise, SPIDER will also be able to characterize the foreground contribution to the B-mode signal. Figure 2 shows the expected dust contribution to the B-mode power at 94 and 150 GHz in the SPIDER observing region, based on the model shown in the left panel of Figure 1. A relatively large band of uncertainty is also shown, based on the assumption that current models may be under-estimating the amplitude of polarized dust at high latitudes.[18, 24] If r is large, SPIDER will be able to distinguish the primordial signal from dust at degree scales by leveraging data from both frequency bands. If r is relatively small, SPIDER should provide a high fidelity map of high-latitude foreground emission at the CMB frequencies. A subsequent flight of SPIDER with instruments at higher frequencies will then allow foreground separation over the cleanest parts of the high-latitude sky, and enable detection of primordial signals above the $r \sim 0.03$ level.[20] Frequency selection and further optimization of the observing region will be informed by the final release of polarization data from the *Planck* team. The ballooning platform allows access to a wide range of frequencies without significant atmospheric contamination, so frequencies higher than those typically accessible from the ground ($\gtrsim 220$ GHz) will be considered.

3. INSTRUMENT OVERVIEW

3.1 Receiver

SPIDER was designed to be a relatively modular instrument, with room for six independently controlled receivers, one of which is shown in Figure 3. The design of the receivers is discussed in more detail in Runyan (2010).[25] The optical system is a simple refractor, as originally designed for the the BICEP1 instrument.[26] The aperture
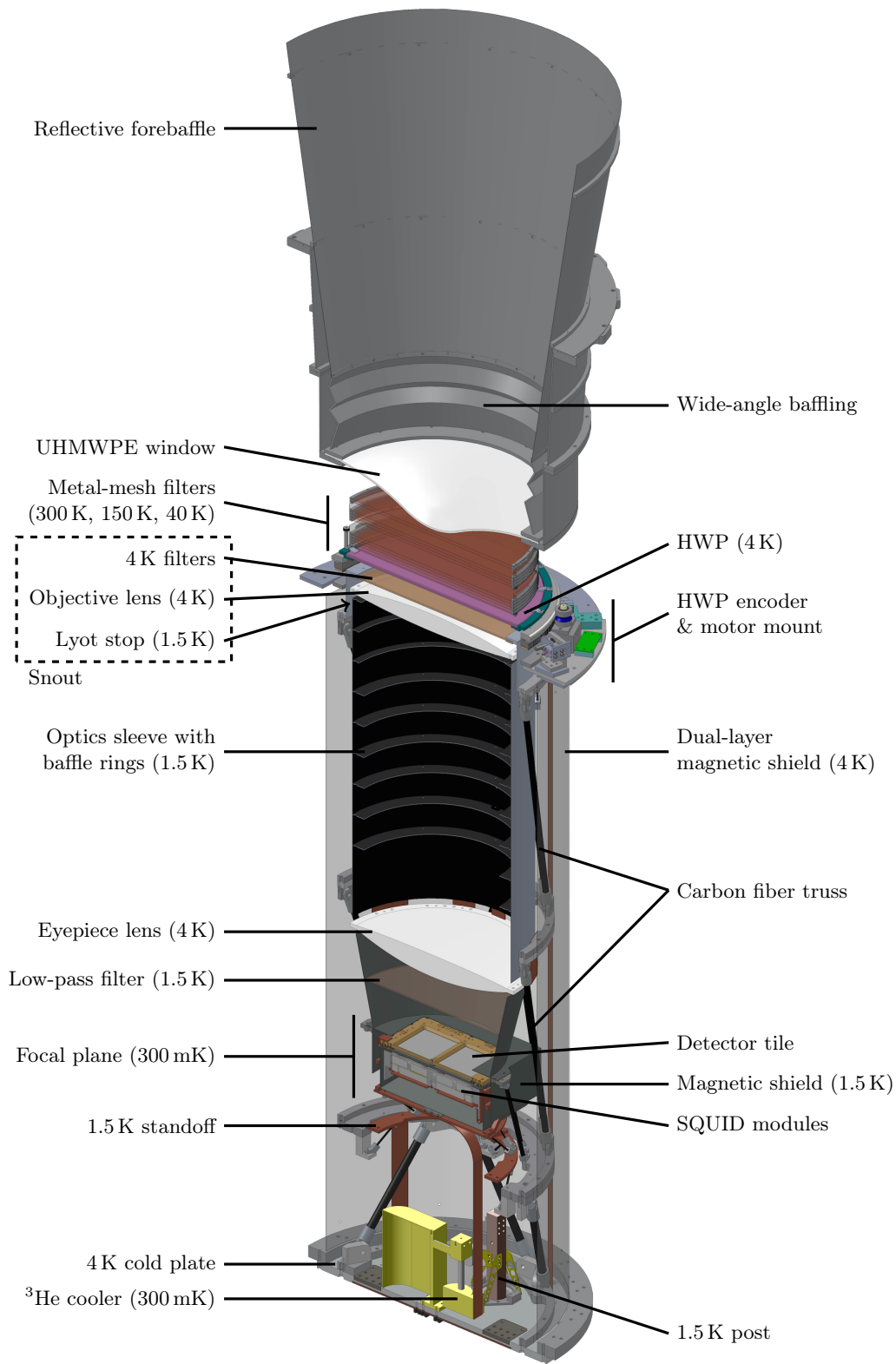
Figure 3. A section view of the receiver, showing the refractive optics, filters, baffling, and focal plane assembly.

Labels:
- Reflective forebaffle
- Wide-angle baffling
- UHMWPE window
- Metal-mesh filters (300 K, 150 K, 40 K)
- HWP (4 K)
- 4 K filters
- Objective lens (4 K)
- HWP encoder & motor mount
- Lyot stop (1.5 K)
- Snout
- Optics sleeve with baffle rings (1.5 K)
- Dual-layer magnetic shield (4 K)
- Carbon fiber truss
- Eyepiece lens (4 K)
- Low-pass filter (1.5 K)
- Detector tile
- Focal plane (300 mK)
- Magnetic shield (1.5 K)
- SQUID modules
- 1.5 K standoff
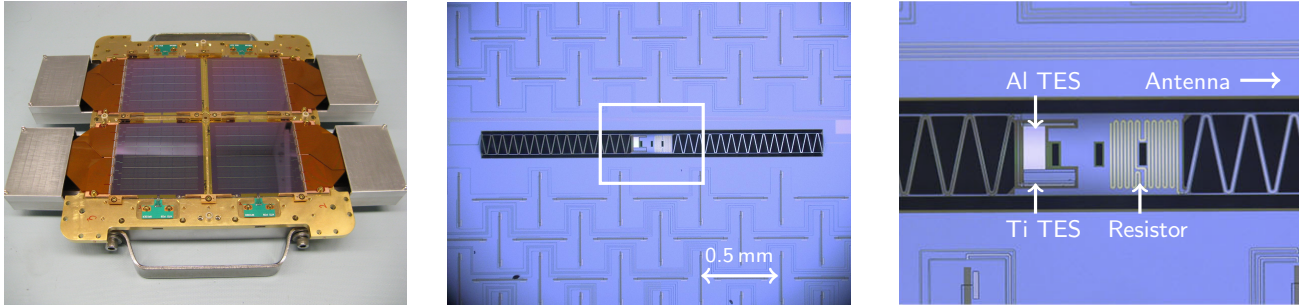- 4 K cold plate
- ^{3}He cooler (300 mK)
- 1.5 K post

Figure 4. (*left*) The underside of a fully populated SPIDER 150 GHz focal plane during assembly, with the 8×8 grid of pixels visible on each of the four tiles. (*middle*) A microscope image of a bolometer island and surrounding dipole antenna array. (*right*) A close-up image of the island, with both TES devices and the meandering gold resistor clearly visible.

of each receiver is 25 cm with a 20° field of view, optimized for degree-scale resolution on the sky. The window for each aperture is a relatively thin (1/8") ultra-high molecular weight polyethylene (UHMWPE) sheet, anti-reflection (AR) coated for the appropriate frequency band. The window is mounted in a reentrant "bucket" which accommodates a lightweight reflective baffle protecting the telescope from stray rays outside of its 20° field-of-view. A carbon-fiber structure provides rigid support of the focal plane and lenses with minimal coefficient of thermal contraction, to avoid distortion of the beam. The high-density poylethylene (HDPE) lenses are simple conics in a telecentric configuration to allow a straightforward mapping of the flat focal plane onto the sky, and are cooled to 4 K to reduce in-band loading due to dielectric loss. A blackened sleeve placed between the two lenses is cooled to 1.5 K to further reduce instrument loading, and also provides a beam-defining Lyot stop just below the objective lens. Infrared loading is attenuated by an AR-coated $10 \, \mathrm{cm}^{-1}$ metal-mesh filter and an AR-coated 1/8" nylon dielectric filter, placed in the "snout" above the objective. An independently-controlled sapphire half-wave plate (HWP) is mounted above the snout on each receiver for modulating polarization on the sky.[27] An Amuneal® Amumetal-4K magnetic shield cooled to 1.5 K surrounds the focal plane and supports a final low-pass metal-mesh filter ($4 \, \mathrm{cm}^{-1}$ and $6 \, \mathrm{cm}^{-1}$ for 94 and 150 GHz, respectively) and above the detectors. The AR-coatings and filters are all individually optimized for the SPIDER frequency bands. The focal plane is stood off from the 1.5 K stage using a smaller carbon-fiber structure, and cooled to 300 mK using a closed-cycle helium-3 adsorption refrigerator. Stainless steel passive thermal filters reduce responsivity to thermal fluctuations in the fridge, with a time constant of about 80 seconds. Flexible copper heat straps provide thermal contact to the refrigerator condensation point (1.5 K) and cold head (300 mK), while solid copper bus bars along the length of the receiver maintain a low thermal gradient between the cold plate and the snout.

3.2 Focal Plane

The focal plane and cold readout electronics have been optimized for a sensitive polarimetric measurement at millimeter wavelengths.[28] Both the beam-forming and bolometric elements of the detectors are lithographed in a grid pattern onto an SiN wafer, as shown in Figure 4. Each physical pixel consists of two detectors, one of which is sensitive to vertical polarization, and the other of which is sensitive to horizontal polarization. The detector beams are formed by an interleaved array of horizontal and vertical slot dipole antennas, with each polarization fed via microstrip lines to independent bolometer islands. The bolometers are superconducting transition-edge sensors (TES) with thermal conductivities tuned for balloon-borne observations. Each bolometer island contains a meandering gold resistor onto which power from the antennas is dissipated, a titanium TES ($T_c \sim 500 \, \mathrm{mK}$, $R_n \sim 30 \, \mathrm{m\Omega}$) with a typical saturation power of ~2-3 pW for science observations in flight, as well as an aluminum TES ($T_c \sim 1.1 \, \mathrm{K}$, $R_n \sim 0.1 \, \Omega$) with a saturation power of ~80 pW which allows ground-based end-to-end testing of the optical systems using $\mathrm{LN_2}$ or room-temperature sources.

The detectors are read out using a three-stage superconducting quantum interference device (SQUID) system with time-domain multiplexing electronics.[29] The layout of the focal plane and SQUID modules was designed to accommodate a multi-layer magnetic shielding architecture, necessary for SPIDER's wide-area scan and motion within the Earth's varying magnetic field. The expected shielding factor of this design is 10^8, an order of magnitude better than necessary to maintain stable detector operation.[25]
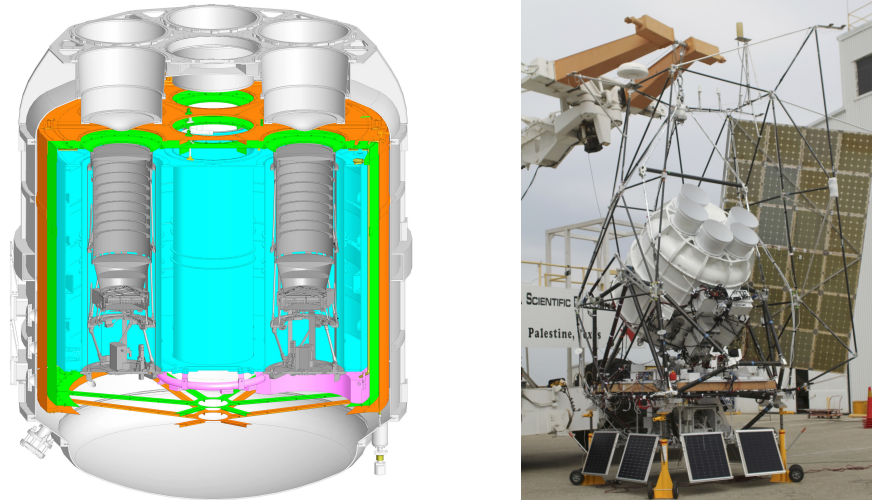
Figure 5. (*left*) The cryostat with each temperature stage highlighted: VCS2 (orange), VCS1 (green), main tank (cyan), and superfluid tank (pink). The receivers (dark gray) are shown in detail in Figure 3. (*right*) The cryostat mounted on the fully assembled gondola during the 2013 integration campaign.

3.3 Cryogenic System

The SPIDER receivers are housed in a large (2 m diameter) liquid helium cryostat,[30] shown in Figure 5. The main tank (hereafter MT) can hold up to 1300 L liquid He, and provides 4 K cooling power to each receiver via flexible copper straps in addition to a thermal bus running internally to the cryostat. The main tank also supplies liquid to the pumped auxiliary superfluid tank (hereafter SFT) via a custom-designed capillary system (Section 4.3). The SFT provides a 1.5 K condensation point for each of the closed-cycle helium-3 adsorption refrigerators inside each receiver. The boil-off vapor from the main tank also provides cooling power to two vapor-cooled shielding stages (VCS1 and VCS2) via a series of heat exchangers. Multi-layer insulation (MLI) between the vacuum vessel wall and each of the VCS stages reduce radiative loading on the colder stages. The receiver apertures at each VCS stage are covered with a combination of single and multilayer reflective low pass metal-mesh filters,[31, 32] designed to minimize infrared loading on the cryogenic system, while maintaining adequate microwave throughput to the detectors (Section 4.2). This system is designed to provide more than 20 days of hold time under flight loading conditions. Temperature control and monitoring is provided by custom housekeeping electronics.[33]

3.4 Gondola and Pointing Systems

The cryostat is supported on a light-weight carbon fiber gondola,[34] along with the flight electronics, pointing sensors and motors, and communications equipment. The gondola is able to point the receivers using a combination of a reaction wheel and pivot for azimuth control and a pair of linear actuators for elevation control.[35] The pointing system was designed to scan in azimuth with a sinusoidal velocity profile, providing speeds of up to 6 deg/s, and accelerations up to 0.8 deg/s^2. A variety of sensors are used to determine the in-flight and post-flight pointing solution.[36] A differential GPS, a magnetometer, pin-hole sun sensors, clinometers and elevation encoders are used to reconstruct the in-flight pointing solution to an accuracy of a few minutes of arc. Post-flight pointing reconstruction is done using images from an orthogonal pair of tracking star cameras, a boresight star camera, and a 3-axis gyroscope, with an ultimate accuracy of about 3 arcsec. The monitoring and control of the pointing and cryogenic systems are done using custom electronics and software built on the legacy of the BLAST and BLASTpol control systems.[33, 37]

3.5 Scan Strategy

The nominal SPIDER scan strategy was designed to maximize coverage over the largest amount of accessible clean sky in the southern hemisphere. The scan region is limited in right ascension by proximity to the Galaxy or the sun, and in declination by the payload's latitude and the extension of the elevation arms. A sinusoidal scan profile was chosen to limit the amount of torque that the gondola and flight train must exert.[35] The boresight
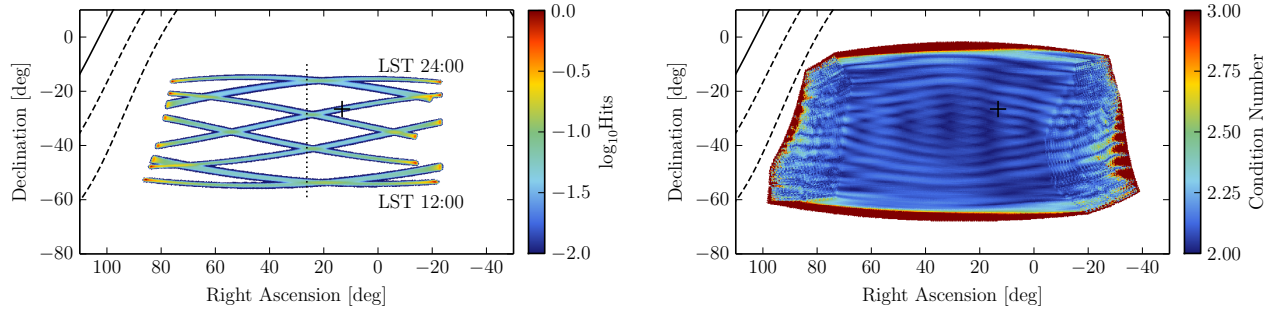
Figure 6. (*left*) The scan pattern for a single detector on the sky over the course of one sidereal day. A five-minute period every three hours is shown. Each back-and-forth scan period in azimuth goes through a track point at the center of the scan region (dotted line). The track point is adjusted for uniform coverage in declination over a twelve-hour period. The lowest track point declination is achieved near sidereal noon, and the highest near sidereal midnight. Sky rotation provides good cross-linking between the upward- and downward-moving half-day scans. (*right*) Combined with 22.5° steps of the HWP every 12 sidereal hours, uniform polarization angle coverage is achieved throughout the map, as evidenced by the condition number of the pointing matrix for a full 256-pixel/512-detector focal plane. The condition number is 2 in the limit of ideal angular coverage. Galactic latitudes $b = 0°$ (solid), $b = -10°, -20°$ (dashed), and the southern Galactic pole ($+$) are also shown in each panel.

motion across the scan region at different times of the sidereal day is shown in Figure 6. Later in the summer season (late December to January) the sun moves closer to the Galaxy and restricts the available sky with low foreground contamination, so an early launch is favorable for SPIDER. Rotation of the sky within the field of view provides good angular cross-linking across the extent of the map, as long as the payload remains at latitudes of about $-80°$ or higher as it follows the circumpolar winds around the continent. To further improve angular coverage, the HWP is stepped by 22.5° every 12 sidereal hours.

For reconstruction of the I, Q and U Stokes parameters from the detector time streams, a set of linear equations is constructed for each map pixel:[38]

$$
\begin{pmatrix} \langle d \rangle \\ \langle d\gamma \cos 2\psi \rangle \\ \langle d\gamma \sin 2\psi \rangle \end{pmatrix} = \begin{pmatrix} 1 & \langle \gamma \cos 2\psi \rangle & \langle \gamma \sin 2\psi \rangle \\ \langle \gamma \cos 2\psi \rangle & \langle \gamma^2 \cos^2 2\psi \rangle & \langle \gamma^2 \cos 2\psi \sin 2\psi \rangle \\ \langle \gamma \sin 2\psi \rangle & \langle \gamma^2 \cos 2\psi \sin 2\psi \rangle & \langle \gamma^2 \sin^2 2\psi \rangle \end{pmatrix} \begin{pmatrix} I \\ Q \\ U \end{pmatrix},
\tag{1}
$$

where the data d are noisy observations of the microwave sky, $\langle \ldots \rangle$ indicates an average over time stream elements falling into the map pixel, γ is the polarization efficiency of the given channel, and $\psi = \phi + 2\theta$ is the projected polarization angle onto the map pixel, with detector angle ϕ and additional rotation 2θ provided by the HWP. Many methods have been developed for optimal inversion of these equations. Additionally, the inversion becomes more complicated if non-idealities in the HWP must be taken into account.[39] However, we can make a simple estimate of how well the Stokes parameters can be reconstructed by estimating the condition number of the matrix in equation 1 (the ratio of the largest and smallest singular values of the matrix), shown in Figure 6 and averaged over all detectors on a focal plane over a single sidereal day of observation, in the ideal scenario of an ideal HWP and $\gamma = 1$. In the limit of perfect angular coverage, i.e. if both the Q and U Stokes parameters are measured with equal sensitivity, the condition number should approach 2; thus, the scan strategy as designed is quite uniform and near ideal.

The scan strategy naturally divides a single day's observation into two halves: the upward-moving scan before sidereal midnight, and the downward-moving scan after sidereal midnight. The same scan is repeated each day, with a different pair of HWP angles during each half of the day. Observation over eight days, at all eight unique HWP angles during each half day, provides an optimal set of maps from which to correct for systematic effects, most notably beam systematics or ghosting, by taking appropriate linear combinations of half-day maps to create templates or subtract out these effects.[40]

The modularity of the instrument and scan strategy lend itself very naturally to a large selection of null tests to probe systematic effects. An angular power spectrum of the difference between two halves of the dataset, when compared against simulations of expected variation in the signal and noise, should yield a spectrum consistent with a null result, if all instrumental and systematic effects are well understood. Table 2 lists a selection of such

Table 2. A selection of null tests that can be performed on the Spider dataset to probe various systematic effects.

Null Test	Systematics Probed
Upward-moving vs downward-moving	transfer function, gain drifts, ground pickup
Left-moving vs right-moving	transfer function, galactic sidelobes
Inner pixels vs outer pixels	beam ellipticity, ghosting, sidelobes
A pol vs B pol	cross-polar leakage
Left tiles vs right tiles	sidelobes
Even rows vs odd rows	electrical cross-talk
94 GHz vs 150 GHz	foregrounds
Left receiver vs right receiver	gain drifts, sidelobes, polarization offsets
Early days vs late days	gain drifts

consistency tests. This is by no means an exhaustive list, but is meant to illustrate the discriminatory power of the Spider dataset.

4. CRYOGENIC PERFORMANCE

4.1 Equilibrium Performance and Hold Time

The SPIDER cryostat's main tank (MT) can hold up to 1300 L of liquid helium. It was designed to stay cold throughout a long duration balloon flight, which typically last from 10 to 20 days. Recent testing with all six receiver ports populated indicates equilibrium temperatures of 40 K and 150 K at VCS1 and VCS2, respectively. The equilibrium gaseous flow rate is ∼40 SLPM through the VCS heat exchangers, corresponding to a load of about 2.5 W. This indicates an expected hold time of roughly 16 days. Prior testing with one or two populated receivers indicated a 40% lower load on the MT. The reduced hold time is thought to be due in part to increased radiative loading through the apertures, discussed in more detail in the following section.

4.2 Radiative Filtering

The Spider filter stack was designed to be effective under ground loading conditions, where the incident radiation is typically a 300 K blackbody peaking at ∼16 THz, and float loading conditions, where the incident radiation is the 2.7 K CMB blackbody above an emissive atmosphere. A combination of thick dielectric filters, thin metal-mesh reflective shaders,[31] and multi-layer hot-pressed metal-mesh filters[32] are used to achieve the desired in-band loading on the detectors and infrared loading on the system. A detailed model of the transmission and absorption of these filters was used to inform modifications for improving cryogenic performance.

4.2.1 Window

The vacuum is maintained by a ⅛" ultra-high molecular weight polyethylene (UHMWPE) window, with an anti-reflection coating (Porex® PM23DR) applied to both sides. An excess load has been observed on the cryogenic system, some of which could be due to the emissive window. Because the potential for light leaks down the optical path is high, cutting off the load from the window before it reaches the colder stages is expected to improve cryogenic performance. To reduce infrared loading on the VCS stages from the window, a pair of baffled shaders have been installed directly below the window; the effect of these shaders on cryogenic performance will be evaluated in upcoming testing prior to deployment. Near the detector passbands, the window is expected to contribute about 0.1 pW to the internal load on the detectors.

4.2.2 VCS1 and VCS2

The VCS2 temperature stage typically reaches about 150-160 K, which is too hot to support any absorptive filters, so only single-layer IR shaders are installed. Four shaders provide a 1 THz cut-off with 90% passband transmission and < 5% stopband transmission. The load onto VCS2 is expected to be about 2 W per aperture, and transmit about 1% of the incident radiation on to VCS1.

The VCS1 stage houses three additional shaders and a 12 cm^{-1} multi-layer filter. To further attenuate radiation above 1 THz, an AR-coated nylon filter was considered; however at the nominal ∼40 K temperature of
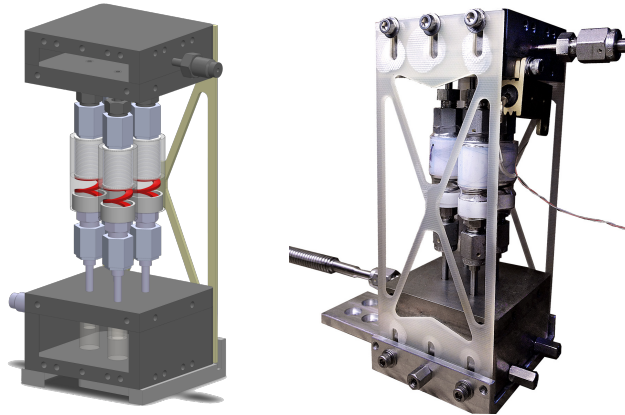
Figure 7. A section view of the capillary assembly (left) and completed structure (right). Four capillaries connect the 4 K main tank box (bottom) to the 1.6 K superfluid box (top). The double volume structure is supported by two ⅟₃₂" thick G10 flexures. The thermal load conducted through these flexures is negligible compared to the cooling power from the superfluid ^{4}He. Porous stainless steel Mott filters located below each capillary prevent ice and other dirt from entering and clogging this high impedance tubing. Superfluid helium exits the capillaries in the smaller of the two boxes (top) which is connected to the superfluid tank through 6" long bellows tubing with a ⅛" diameter.

the VCS1 stage, modeling of the nylon filter suggested it could be emitting as much as 70 mW (∼400 mW for all six receivers), which represents a substantial fraction of the load onto the main tank; removal of this filter was seen to improve cryogenic performance in recent testing.

4.2.3 Receiver Filters

Additional filters are installed within each receiver assembly. A 10 cm^{-1} AR-coated multi-layer low-pass filter is the top-most 4 K filter to reflect the majority of infrared radiation. An AR-coated nylon filter is placed just below that to attenuate any blue leaks above 1 THz. A 6 cm^{-1} low-pass filter (4 cm^{-1} in the 94 GHz receivers), installed within the 2 K magnetic shield, defines the upper edge of the detector passband. The total in-band loading onto the detector has been measured in a test system to be about 0.5 pW,[41] consistent with expectations from modeling of the filter stack. Additional baffling, discussed in detail in Section 5.2.2, should significantly limit excess loading beyond this.

4.3 Superfluid Capillary

The SPIDER capillary system (Figure 7), based on a classic design,[42] provides continuous flow of liquid ^{4}He from the main tank to the superfluid tank. The system is critical for a successful flight because the hold time of the SFT, when fully charged, is only 4 days, compared to the goal 20 day flight duration. The capillary system has been characterized extensively during cryogenic testing of the flight cryostat. The system provides approximately 100 mW of cooling power to the superfluid tank, which is sufficient to cool six telescopes down to 1.6 K while sustaining daily fridge cycles. The net cooling power can be changed by simply altering the length of the capillaries in a way that does not require any other change to the design. This has allowed us to arrive at an optimal cooling power by having a collection of interchangeable capsules. We find that measurements of 300 K flow impedance is an adequate predictor for superfluid flow rates.[43]

4.4 Sub-Kelvin Systems

Each receiver is cooled to 300 mK with an independently controlled single-stage closed-cycle ^{3}He refrigerator made by Chase Cryogenics. One such refrigerator requires about two hours to recycle at an elevation of 40°, and the system can comfortably handle cycling six such refrigerators with a wait time of about 30 min between each cycle start (Figure 8). The total cycling procedure takes about 4-5 hours to complete, but the focal plane temperatures are not affected by neighboring cycles. The hold times of the fridges are typically in excess of 48 hours. Accounting for non-observing time for tuning and calibrations, we can make a pessimistic estimate of a duty cycle of 85%, which is in line with our design goal.
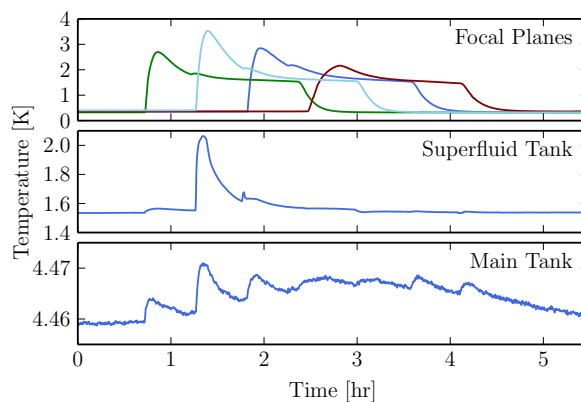
Figure 8. A time stream of thermometry data while cycling four ³He refrigerators. The cycles are staggered half an hour apart, as seen at top, to maintain a manageable load on the SFT. The load on the MT is negligible, and though the SFT temperature increases, it returns to equilibrium quickly. The large 0.5 K rise in the SFT temperature at hour 1.3 is due to the proximity of the thermistor to that refrigerator's condensation point, which heats temporarily when the ³He gas is first released at the beginning of the cycle.

4.5 Cooldown Procedure

In addition to improvements to the radiative filtering, we have optimized the close-up and cooling procedure to ensure optimal performance of the cryogenic systems. The initial evacuation of the vacuum chamber is critical for removing water vapor and other particulates that can degrade the performance of the MLI and introduce excess loading when the system is cold.[44] Upon sealing up the vacuum vessel, we perform at least three purge cycles with dry nitrogen gas; this has been shown to improve the ultimate vacuum pressure that is reached prior to filling with cryogens. Reaching vacuum pressures of $\mathcal{O}(10^{-3})$ torr prior to filling cryogens takes at least three days due to the large volume and out-gassing surface area of the system. Once a low vacuum pressure is reached, the main tank is filled with $300-400$ L of liquid nitrogen to pre-cool the VCS layers and receivers; the time to equilibrium is approximately another three days. The SFT is maintained at a pressure of 5 psi above atmosphere using dry helium gas, to prevent the capillary lines from clogging with LN_2 or water vapor, and cools radiatively during this period. Finally, the LN_2 is removed by pressurizing the main tank, and replaced with liquid helium. The SFT is evacuated with a roughing pump and rapidly cools to below the 2.2 K λ-point of ⁴He once steady liquid flow is established. Final equilibrium temperatures are reached in another $3-4$ days, at which point the refrigerators are ready to cycle for operation of the detectors. In total, the vacuum pumping and cooldown to operational temperatures requires about two weeks to complete.

The system will be launched with the detectors cold and operational, and with the SFT evacuated. A low-power diaphragm pump will be powered up shortly before launch, to replace the roughing pump during ascent and maintain the SFT pressure below ∼100 torr. Upon reaching float altitude (∼35 km), the diaphragm pump will be bypassed in favor of the low-pressure atmosphere, by commanding a pair of motorized bellows valves.

The cryogenic systems have been thoroughly tested in preparation for flight, and found to perform adequately for our science goals.

5. TELESCOPE PERFORMANCE

5.1 Detector Characterization

The noise performance of the detectors has been well characterized in the flight cryostat under flight-like loading conditions. We expect the sky loading in flight to be an effective 4-5 K source (including the CMB and the atmosphere), which can be simulated on the ground by covering the focal plane at the 4 K snout with an aluminum plate. In a smaller test cryostat, flight-like loading can be simulated using a temperature-controlled liquid ⁴He cold load attached at the window aperture, and has been used to accurately measure instrument loading and optical efficiency on the titanium devices.[41, 45] As an alternative to the cold load, a removable curved mirror
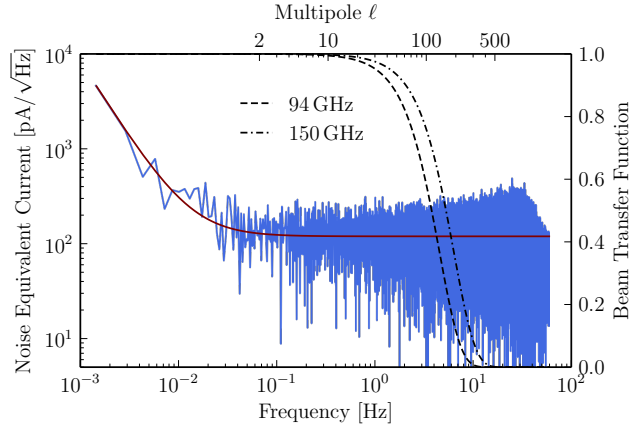
Figure 9. Amplitude spectral density of a typical detector in current units, with a fit to a spectral shape including $1/f$ and Gaussian noise components. For typical scan speeds of 6 deg/s, the noise is relatively flat over the angular scales of interest ($10 < \ell < 300$), where $\ell \sim f\,v_{\text{scan}}/180°$. Note that the excess amplitude above 10 Hz is outside of the beam transfer function at these scan speeds. This excess noise is believed to be due to the distributed heat capacity in the long meandered legs leading up to the bolometer island.[28]

at the window can be used to present an effective 10-20 K load, just under the saturation temperature of the titanium devices.

The shape of the noise spectrum on a typical time-domain multiplexed device has been measured in various test systems.[41, 45] The detector sample rate is limited by the capacitance of over 3 meters of cryogenic cabling between the multi-channel electronics (MCE) crate and the focal plane. The SPIDER switching rate between channels is 470 kHz, which gives a per-channel sample rate (after on-board decimation) of 120 Hz. A typical noise spectrum is shown in Figure 9, acquired in the flight system with the detector biased on the titanium transition at $R \sim 0.7 R_n$. This bias position is chosen to minimize noise-equivalent power (NEP) on transition, as estimated from the noise plateau in the ~2-8 Hz range. At typical scan rates of 6 deg/s the noise is relatively white over the angular scales of interest ($10 < \ell < 300$).

To determine the signal-to-noise on the sky, the noise-equivalent current (NEI) on the detector must be converted to noise-equivalent temperature (NET) referenced to the input signal:

$$\text{NET} = \text{NEP}\,\frac{dT}{dP_{\text{opt}}} = \text{NEI}\,\frac{dP_{\text{opt}}}{dI_s}\frac{dT}{dP_{opt}}, \tag{2}$$

where I_s is the current signal, dI_s/dP_{opt} is the detector responsivity to an optical signal, and dP_{opt}/dT is the
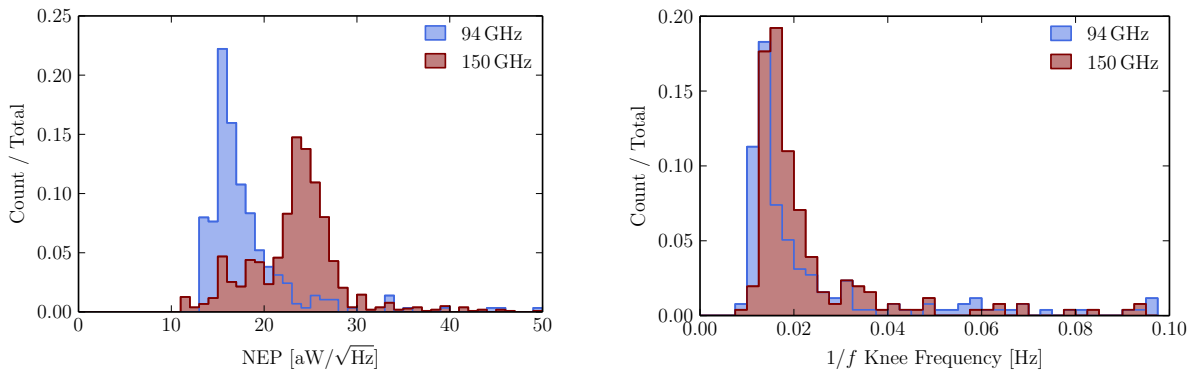

Figure 10. (*left*) Histogram of NEPs for a representative subset of 94 GHz and 150 GHz detectors, measured during a period of 15 minutes of quiescent data acquisition while looking at a 4 K load in the flight system. These NEPs correspond to NETs of about $120\,\mu\text{K}\sqrt{s}$ and $140\,\mu\text{K}\sqrt{s}$, respectively. (*right*) Histogram of $1/f$ knee frequencies during the same acquisition period.
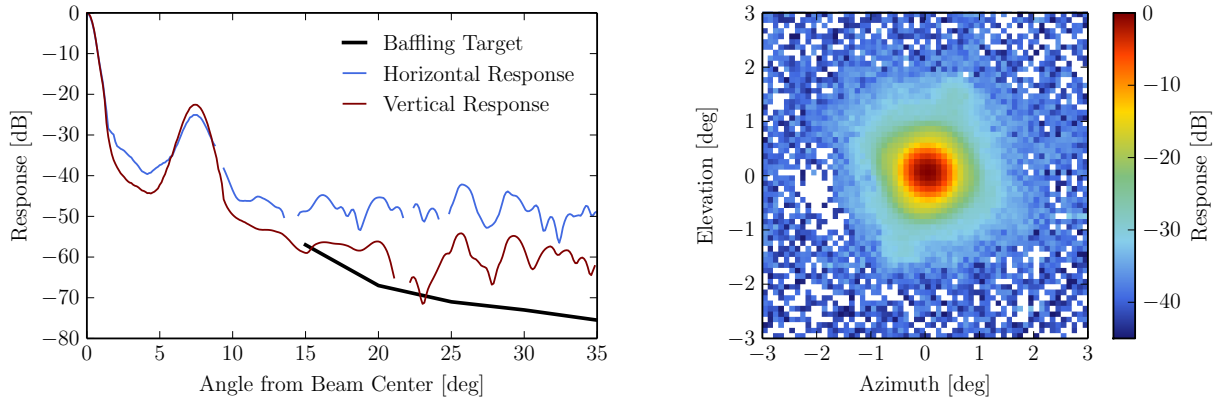
Figure 11. (*left*) A slice through a single 150 GHz beam with both horizontal and vertical polarizations, acquired using a polarized source in the far field. A ghost beam is evident 8° away from the beam center, due to reflections off of elements along the optical path. The forebaffle attenuates the signal beyond about 10°, so the sidelobes appear to be below the noise floor in this dataset. The target level of sidelobe attenuation (black) was determined from a set of simulations of a SPIDER scan across a sky with Galactic emission.[20] (*right*) Stacked beams on a 150 GHz focal plane, with cross-talk beams between neighboring pixels visible above and below the main beam. The orientation of these secondary beams indicate that the focal plane was rotated with respect to the elevation axis by 22.5°. These data were acquired during scanning tests of the fully integrated system in Palestine, TX, with the pointing solution reconstructed by integrating the 3-axis gyroscope signal.

system optical efficiency. For fast detectors (loop gain $\mathcal{L}_I \gg 1$, time constant $\tau \sim 1\,\mathrm{ms}$), we can use the DC approximation in the large loop gain limit, and the optical responsivity scales linearly with the electrical responsivity:[46]

$$\left.\frac{dI_s}{dP_{\mathrm{opt}}}\right|_{\omega=0} = \frac{1}{I_b R_L}\left(2\left.\frac{dI_s}{dI_b}\right|_{\omega=0} - 1\right) = \frac{2\eta|_{\omega=0} - 1}{I_b R_L}, \tag{3}$$

where I_b is the bias current (typically $\sim 100\,\mu\mathrm{A}$), and R_L is the load resistor in the voltage-biased TES circuit ($3\,\mathrm{m}\Omega$). This linear relation has been verified for the SPIDER detectors with a chopped thermal source placed at the aperture. The second equality above defines the electrical responsivity η, which can also be written in this limit in terms of the TES resistance R as

$$\eta|_{\omega=0} = -\frac{R_L}{R - R_L}. \tag{4}$$

The electrical responsivity can be quickly measured by stepping the TES bias current by a known small amplitude at a relatively low frequency ($\sim 1\,\mathrm{Hz}$), and measuring the amplitude of the signal current. These electrical "bias steps" enable efficient monitoring of the detector NEP in flight, and are discussed further in Section 6.3.3. Histograms of typical plateau NEP values and the knee frequency of the $1/f$ component are shown in Figure 10, and indicate relatively quiet and stable performance of the detectors.

5.2 Optical Characterization

5.2.1 Beams

The detector main beams have been extensively measured in a test system, mounted on an azimuth-elevation pointing system and scanning a thermal source near the far field ($\sim 30\,\mathrm{m}$). The beam widths have been measured to be 42 arcmin at 94 GHz and 30 arcmin at 150 GHz, with differential beam parameters (width, ellipticity, centroid offset) at the 1% level or below.[45]

Sidelobes have been characterized using wide-angle scans pointed at an amplified polarized source, and are currently limited by the brightness of the source. A slice through a single detector's beam (Figure 11) shows the response of each polarization in a single physical pixel. Also evident is a "ghost" beam about 8° from the beam center, which is a typical consequence of reflections off of optical elements in a refractive configuration. This ghost has been measured at an amplitude of $\sim 1\%$. The ghost location depends on the location of the pixel within the focal plane; this particular ghost is for a pixel located about 3-4 degrees from the bore-sight.
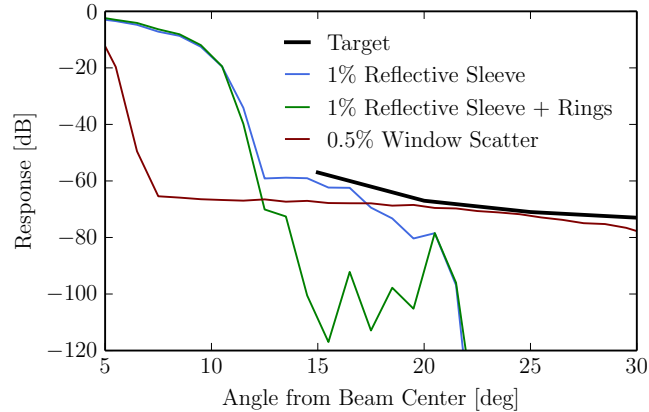
Figure 12. Zemax® modeling of attenuation of 100% polarized sidelobes by internal and external baffling, at a pixel near the edge of the focal plane, where pickup is expected to be strongest. The target level of attenuation (black) is also shown in Figure 11. If both horizontal and vertical polarizations are attenuated to at least this level, then excess sidelobe pickup is expected to be sub-dominant to a primordial B-mode signal at $r = 0.03$.[20] Optical simulations of a 1% reflective sleeve with (green) and without (blue) baffle rings along the length of the sleeve indicate adequate attenuation. Simulations of 0.5% Lambertian scattering off the window, include the forebaffle design shown in Figure 3 and a completely absorptive optics sleeve, indicate marginal performance beyond ∼20°. The combination of the external forebaffle and the blackened internal sleeve should limit the observed sidelobe pickup to acceptable levels, especially in the more realistic scenario that the sidelobes are only partially polarized.

Signal pick-up ("cross-talk") between neighboring detectors has also been characterized. Figure 11 shows a 150 GHz beam produced by stacking all detectors on the focal plane. The upper and lower cross-talk beams are visible at about the −25 dB level, aligned with the focal plane axes (−22.5° relative to the elevation axis).

All of these beam effects have been simulated[20, 47, 48] and are expected to contribute negligible levels of spurious B-mode power at these amplitudes (relative to an $r = 0.03$ primordial signal). Moreover, rotation of the HWP provides a robust way of minimizing sensitivity to these beam effects. Rotation of the polarization angle on the sky without displacing the beam centroid enables the creation of daily maps in which these beam effects contribute with opposite sign, and can thus be easily separated from the signal.

5.2.2 Sidelobes and Baffling

Simulations of sidelobe pick-up of Galactic emission indicate that the attenuation requirement for SPIDER is quite strict in order to reduce the spurious B-mode contribution to well below a $r = 0.03$ primordial signal.[20] The attenuation target is shown in Figure 12. To reach this target, we have built on the baffling scheme typically used by the ground-based BICEP-style experiments.

The SPIDER forebaffles are designed to prevent contamination from polarized sources, including reflections from the balloon and ground and wide-angle Galactic emission. The strongest constraint on the design of the forebaffles comes from the spacing of the individual receivers. To stay outside of the beam and not interfere with neighboring baffles, simple conical forebaffles can extend only 26 inches from the vacuum window. Simulations show that this is enough to reduce balloon and ground pick-up to acceptable levels, so a more complicated design is not necessary. The forebaffles are reflective, because absorbing baffles were measured to contribute unacceptable levels of detector loading (nearly 1 pW) prior to the introduction of the 2 K sleeve internal baffles described below. Lab measurements indicate less than 0.3 pW of loading from each forebaffle at both 94 and 150 GHz. The sidelobe power is dominated by a combination of window scattering and optics sleeve reflections. The AR-coated UHMWPE windows scatter less than 0.5% in our bands. To reduce the amount of scattered light reaching wide angles on the sky, the lower section of each forebaffle features a zig-zagged portion, optimized to reflect some of these rays back into the cryostat.

Reflections from the 2 K sleeve have also been observed to contribute strongly to the sidelobe power. The optics sleeve has typically been blackened with steel- and carbon-loaded STYCAST®, but this coating has been found to be as much as 80% reflective for ∼2 mm thicknesses at shallow angles. A surface at least 5 mm thick would be required to reduce reflections to below 15%. To stay within mass constraints, we have instead covered
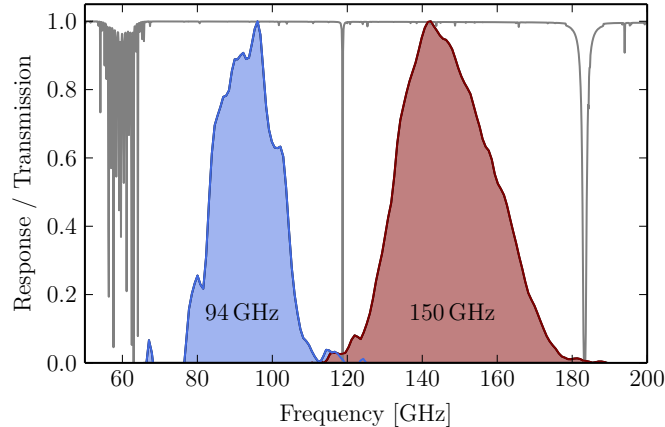
Figure 13. Average spectral response of the 94 GHz (blue) and 150 GHz (red) detectors. These spectra correspond to a 24% bandwidth at both frequencies. The bands were placed to avoid the 60 GHz and 180 GHz water vapor resonances, and the 120 GHz oxygen resonance that are present in the atmospheric transmission spectrum at 30 km altitude (gray).

the sleeve with Eccosorb® HR-10 material, which should ensure 1% reflectivity at microwave frequencies. In addition to the strongly absorptive material, a series of baffle rings have been placed in strategic locations along the length of the optics sleeve, and optimized to reflect light back into the cryostat. These baffle rings alone have been shown to reduce the loading on each receiver by about 0.2 pW. The unique design of our forebaffle combined with these internal baffle rings allows us to limit our sidelobes to the required levels, as shown in Figure 12.

5.2.3 Bandpass and Optical Efficiency

The spectral bandpass of each detector is defined by both a low-pass filter mounted at the aperture of the 2 K magnetic shield, and a 3-pole LC filter along the microstrip line leading to each bolometer. The bandpass has been measured using a compact polarized Fourier transform spectrometer (FTS) with a chopped thermal source. The average bandpass for both frequencies is shown in Figure 13. The bandwidth is about 24% for both frequencies. No significant mismatch between polarizations has been observed.

The end-to-end optical efficiency of the detectors is determined by biasing on the aluminum transition, measuring the change in bias power between a 300 K and a 77 K (LN_2) load, and comparing to the expected dP/dT for a blackbody source with the observed bandpass. Observed efficiencies are typically about 35-40%, with some channels as high as 50%.

5.2.4 Polarimetric Calibration

Cross-polar response has been limited to 0.5% on typical detector pairs, whose dominant source is multiplexer cross-talk.[49] This measurement was done using a rotating polarized source (RPS) in the near field, peaked on one detector at a time. A complete revolution of the HWP at various fixed RPS angles produced modulation of both detector polarizations, from which the relative orientations of the detectors were determined.

Final polarization calibrations will be tested before deployment, and completed just before launch. We plan to use a rotating polarized grid at the window aperture, to determine the orientations of all of the detectors relative to each other, to the HWP, and to the cryostat reference frame. The requirement for the accuracy of this measurement is about 1° for both relative and absolute angle calibrations,[20] which is easily achievable with the HWP encoder system (accurate to 0.1°).[40]

6. INSTRUMENT INTEGRATION

Full integration of the SPIDER flight system was successfully completed during the summer of 2013 at NASA's Columbia Scientific Ballooning Facility (CSBF) in Palestine, TX. This included assembly of the solar power systems, integration with the NASA telemetry equipment, and integration of the detector control systems with the flight commanding and downlink infrastructure.

6.1 Power Systems

The power systems for SPIDER are based largely on designs used by the BLAST and BLASTpol instruments.[37] The electronics are divided into an inner frame and an outer frame, which are electrically isolated from each other. The inner frame includes the detector readout electronics (one MCE crate per receiver), the cryogenic housekeeping system, and the HWP control system. The outer frame includes all flight computers (one per receiver, and two redundant control computers), peripherals (data storage pressure vessels, serial hub, etc), the pointing control systems, and the line-of-sight telemetry equipment. The cryostat vacuum shell is the electrical ground for the MCEs, and is carefully isolated from the outer frame electronics by means of isolating DC-DC converters.

Two 4×3 arrays of solar panels (SunPower® A-300) provide independent power to the inner and outer frame systems. Solar power from each array is fed to a pair of series 12 V lead-acid batteries (Odyssey PC1200), via a solar charge controller (MorningStar® TriStar MPPT-60). This power system was fully assembled and tested in summer 2013, and is expected to provide up to 2 kW of solar power during flight, with an efficiency of up to 21%.

6.2 Payload Control and Telemetry

On-board control of the SPIDER payload is handled by a pair of redundant flight computers, which communicate with each of the receiver computers, the pointing motors and sensors, and the housekeeping electronics. Data are stored on redundant systems, with at least three copies distributed among various models of spinning hard disks (enclosed in pressure vessels) and solid state drives, to minimize the probability of data loss due to drive failure. A 25 MHz clock synchronizes data between the flight computers and the six MCEs.

Communication with the payload from the ground is facilitated by a Support Instrumentation Package (SIP), provided by CSBF.[50] The SIP allows access to the TDRSS and Iridium satellite networks for communication, as well as a line-of-sight (LOS) transmitter for use during the first 24-36 hours of the flight. Data transmission rates are up to 1 Mbps via LOS, and up to 6 kbps over the horizon, with at the very least a 255-byte packet transmitted every ∼15 minutes. These data rates are too low to allow transmission of the full SPIDER dataset (∼12 Mbps), so only a subset of the data are transmitted during the flight for monitoring. The SIP was installed and tested during the 2013 integration campaign.

6.3 Detector Tuning and Monitoring

SPIDER will be the first payload to fly a time-domain multiplexed detector readout system. In order to monitor and control the over 2000 individual channels given limited downlink bandwidth, we have created a custom infrastructure for quickly determining the health of each receiver in flight. This system includes tuning of the SQUID readout electronics, tuning of the detector responsivity, and monitoring of the detector stability throughout the flight.

The monitoring software runs independently on each MCE computer, and handles acquisition of data onto each of three redundant data drives, communication with the flight computer, and tuning and monitoring of the readout system. The program stores a copy of all runtime parameters on each data drive, from which it can recover the last known working state in the event of loss of communication or power failure.

6.3.1 SQUID Tuning

The detector resistances are read out by a 3-stage system of SQUIDs that inductively couple to the TES bias circuit.[29] The detectors are arranged into 33 rows and 16 columns in the multiplexer circuit. Each column of SQUIDs and TESs is biased simultaneously, while each pixel is sampled by the multiplexer at 14.3 kHz.

The voltage across each SQUID is a periodic function of the magnetic flux through the SQUID loop, with period equal to the magnetic flux quantum. To tune the SQUIDs, the feedback and bias current at each SQUID stage is swept to maximize both linearity and gain of the response over the dynamic range. Once each SQUID stage has been properly tuned by row (first stage) or by column (second and last stages), a lock point is further optimized for each individual channel, based on the composite response through all three SQUID stages.[51]
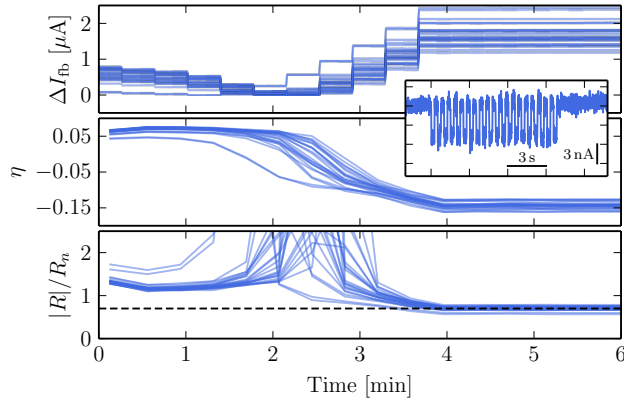
Figure 14. Illustration of automatic detector biasing algorithm. (*top*) Feedback signal for detectors in a single column as the TES bias is adjusted. (*inset*) At each bias level, the bias is pulsed by 1 ADU at 2 Hz and the feedback response is recorded. (*middle*) The measured detector response η is negative when the detectors are on transition. (*bottom*) The effective resistance of each detector (using equation 4), approaches the column average target $R = 0.7R_n$ after several steps.

For ground-based operation, this tuning procedure can be vetted by plotting the response curves for each SQUID and verifying by eye that the chosen lock points are correctly placed along each curve. To remove the user from this procedure, the SPIDER tuning algorithm reduces the SQUID response curves and lock points to a set of statistics (period, slope, amplitude, lock position) for each stage. These statistics are compared against a reference tuning, assuming some allowed thresholds in variation of each statistic. The tuning is successful if the number of failures is below a maximum threshold at each stage. The tuning algorithm will proceed to the next stage on success, or determine some parameters to adjust and repeat on failure. One typical failure mode is a shift in the optimal SQUID bias due to drifts in the SQUID module temperature (common when the liquid cryogen level is low); the algorithm determines the appropriate bias sweep range and finds the optimal bias to maximize the SQUID gain.

Once the SQUIDs are tuned and locked, the detectors are operated in a closed integral servo loop, with the SQUID feedback adjusted in response to changes in the TES resistance. The gain of the integral term has been determined based on the performance of each column to quickly compensate the TES response without inducing runaway oscillations.

A full tuning procedure, to determine both bias and feedback positions for all SQUID stages, typically takes about five minutes per receiver, and will be carried out roughly once per day. To tune just the feedback positions takes about one minute. The latter procedure may be necessary more frequently if magnetic field drifts or cosmic rays should cause the SQUIDs to become unlocked. A new tuning can be triggered by command or if a threshold number of detectors slip out of lock, discussed further in Section 6.3.3.

6.3.2 TES Bias Tuning

Tuning the TES bias can be done by acquiring a load curve for each channel, which is a measure of the current response as a function of bias current. In order to bias the TES on transition starting from a superconducting state, the focal plane must be thermally "kicked" onto transition, because the bias circuit cannot provide enough current to surpass the critical current necessary to drive the detectors normal (above the superconducting transition). Once the detectors on each column are biased and normal, the column bias is ramped down through the superconducting transition, and a bias is chosen such that the NEP on transition is minimized, as discussed in section 5.1. The optimal bias is typically when the detectors are high in the transition, where excess amplifier noise is minimal, so we choose a bias such that the column average TES resistance is 0.7 of the normal resistance R_n.

Acquisition of a full load curve is typically a disruptive procedure, and hysteresis in the focal plane temperature after a kick may indicate a slightly lower bias than is actually necessary. To bias the detectors more efficiently and reliably, we instead take local measurements of the load curve by commanding small periodic ($\sim$1 Hz) steps

on the TES bias lines, and measure the amplitude of the signal response (see Figure 14 inset). The amplitude of the bias step response on transition (η) is related to the TES resistance by equation 4 (Section 5.1). Because η is a smooth function of the TES resistance, the TES bias can be tuned by servoing off of the column averaged electrical responsivity. Figure 14 illustrates how this bias tuning procedure is implemented on a single column. This servoing procedure also naturally allows monitoring of the TES responsivity throughout the flight, as discussed in the next section.

6.3.3 Detector Monitoring

Once the SQUIDs and detectors are tuned and normal data acquisition has begun, a monitoring program ensures that detector performance remains stable. For each receiver, a set of four statistics are calculated at the data frame rate:

Bias step response The TES bias is stepped as discussed in Section 6.3.2, and the responsivity is stored. If the responsivity has changed according to a threshold on the column averaged TES resistance, then the TES bias is adjusted appropriately. Bias steps are acquired at every scan turnaround, and adjusted if necessary roughly every hour.

Mean A channel in oscillation will show a DC mean level that has deviated significantly from zero, indicating a poorly locked channel. This is also a good indicator of a large response to a cosmic ray event or other strong signals.

Noise current The noise current is estimated by taking the RMS of each detector time stream after applying an IIR filter to limit the bandwidth to the plateau region (typically chosen as 2-8 Hz). Combined with the bias step response, this gives an instantaneous estimate of the NEP per channel.

RMS The full-bandwidth noise over a period of about a minute is a good indicator of higher frequency noise, such as RF pickup, or low-frequency $1/f$ noise.

Because full detector time streams are largely unavailable after the LOS period, these statistics provide a means of monitoring detector behavior from the ground, and responding as necessary. To minimize the bandwidth required to transmit these statistics, they are reduced to 8-bit numbers and multiplexed into a single downlink channel. Along with these statistics, each detector is assigned a flag, to which the software is able to respond automatically:

Superconducting / Low / OK / High / Normal The location on transition is determined from the bias step response. The bias is adjusted periodically if too many channels have slipped off of transition. If too many detectors have latched superconducting, then the detectors are kicked back onto transition as necessary.

Clamped In an attempt to prevent oscillatory behavior from affecting neighboring pixels via their common electrical ground, a "clamping" procedure has been implemented at the firmware level on the MCE. This locks the integral term in the error loop to effectively stop the servo before the oscillations can disturb the neighbors. A clamped detector is indicated by a signal time stream that is locked at a constant, non-zero value.

Oscillating A detector with particularly large variation is flagged as oscillating if it is not caught by the clamping procedure. The servo loop can be reset (the integral term re-zeroed) to attempt to stop the oscillatory behavior; if this fails, the gain of the integral servo can be adjusted.

Frail A detector flagged as frail will be reset with a reduced integral servo gain to attempt to stop oscillatory behavior.

Dead If oscillation continues despite the lower gain, the detector can be turned off altogether (zero gain) and flagged as dead.

Thresholds are set for the number of flagged channels; if these thresholds are exceeded, then a new SQUID tuning may be requested, or the MCE may be reset altogether to the last known working state. When only low bandwidth channels are available for downlink, then the statistics are further reduced to a column average, or a simple count of detectors in each flagged state.

This novel detector tuning and monitoring scheme is now used continuously during lab testing, and will enable efficient monitoring and response by the ground crew during flight.

7. CONCLUSIONS

The SPIDER instrument is fully integrated and ready to deploy to McMurdo Station, Antarctica for a December 2014 launch. The telescope performance has been extensively characterized in the flight system. We will observe a large fraction of the southern Galactic sky in an effort to detect the inflationary B-mode signal at degree angular scales. The BICEP2 experiment has observed B-mode power on the sky at these scales,[2] and SPIDER's spatial, angular and frequency coverage make it an ideal instrument for further characterizing the signal's angular spectrum, isotropy and frequency spectrum across the sky.

ACKNOWLEDGMENTS

REFERENCES

[1] Smoot, G. F., Bennett, C. L., Kogut, A., Wright, E. L., Aymon, J., Boggess, N. W., Cheng, E. S., de Amici, G., Gulkis, S., Hauser, M. G., Hinshaw, G., Jackson, P. D., Janssen, M., Kaita, E., Kelsall, T., Keegstra, P., Lineweaver, C., Loewenstein, K., Lubin, P., Mather, J., Meyer, S. S., Moseley, S. H., Murdock, T., Rokke, L., Silverberg, R. F., Tenorio, L., Weiss, R., and Wilkinson, D. T., "Structure in the COBE differential microwave radiometer first-year maps," ApJ **396**, L1–L5 (Sept. 1992).

[2] Ade, P. A. R., Aikin, R. W., Barkats, D., Benton, S. J., Bischoff, C. A., Bock, J. J., Brevik, J. A., Buder, I., Bullock, E., Dowell, C. D., Duband, L., Filippini, J. P., Fliescher, S., Golwala, S. R., Halpern, M., Hasselfield, M., Hildebrandt, S. R., Hilton, G. C., Hristov, V. V., Irwin, K. D., Karkare, K. S., Kaufman, J. P., Keating, B. G., Kernasovskiy, S. A., Kovac, J. M., Kuo, C. L., Leitch, E. M., Lueker, M., Mason, P., Netterfield, C. B., Nguyen, H. T., O'Brient, R., Ogburn, R. W., Orlando, A., Pryke, C., Reintsema, C. D., Richter, S., Schwarz, R., Sheehy, C. D., Staniszewski, Z. K., Sudiwala, R. V., Teply, G. P., Tolan, J. E., Turner, A. D., Vieregg, A. G., Wong, C. L., and Yoon, K. W., "Detection of b-mode polarization at degree angular scales by bicep2," *Phys. Rev. Lett.* **112**, 241101 (Jun 2014).

[3] The POLARBEAR Collaboration, Ade, P. A. R., Akiba, Y., Anthony, A. E., Arnold, K., Atlas, M., Barron, D., Boettger, D., Borrill, J., Chapman, S., Chinone, Y., Dobbs, M., Elleflot, T., Errard, J., Fabbian, G., Feng, C., Flanigan, D., Gilbert, A., Grainger, W., Halverson, N. W., Hasegawa, M., Hattori, K., Hazumi, M., Holzapfel, W. L., Hori, Y., Howard, J., Hyland, P., Inoue, Y., Jaehnig, G. C., Jaffe, A. H., Keating, B., Kermish, Z., Keskitalo, R., Kisner, T., Le Jeune, M., Lee, A. T., Leitch, E. M., Linder, E., Lungu, M., Matsuda, F., Matsumura, T., Meng, X., Miller, N. J., Morii, H., Moyerman, S., Myers, M. J., Navaroli, M., Nishino, H., Paar, H., Peloton, J., Poletti, D., Quealy, E., Rebeiz, G., Reichardt, C. L., Richards,

P. L., Ross, C., Schanning, I., Schenck, D. E., Sherwin, B. D., Shimizu, A., Shimmin, C., Shimon, M., Siritanasak, P., Smecher, G., Spieler, H., Stebor, N., Steinbach, B., Stompor, R., Suzuki, A., Takakura, S., Tomaru, T., Wilson, B., Yadav, A., and Zahn, O., "A Measurement of the Cosmic Microwave Background B-Mode Polarization Power Spectrum at Sub-Degree Scales with POLARBEAR," *ArXiv e-prints* (Mar. 2014). 1403.2369.

[4] Planck Collaboration, Ade, P. A. R., Aghanim, N., Armitage-Caplan, C., Arnaud, M., Ashdown, M., Atrio-Barandela, F., Aumont, J., Baccigalupi, C., Banday, A. J., et al., "Planck 2013 results. XVI. Cosmological parameters," *ArXiv e-prints* (Mar. 2013). 1303.5076.

[5] Hinshaw, G., Larson, D., Komatsu, E., Spergel, D. N., Bennett, C. L., Dunkley, J., Nolta, M. R., Halpern, M., Hill, R. S., Odegard, N., Page, L., Smith, K. M., Weiland, J. L., Gold, B., Jarosik, N., Kogut, A., Limon, M., Meyer, S. S., Tucker, G. S., Wollack, E., and Wright, E. L., "Nine-year Wilkinson Microwave Anisotropy Probe (WMAP) Observations: Cosmological Parameter Results," ApJS **208**, 19 (Oct. 2013). 1212.5226.

[6] Sievers, J. L., Hlozek, R. A., Nolta, M. R., Acquaviva, V., Addison, G. E., Ade, P. A. R., Aguirre, P., Amiri, M., Appel, J. W., Barrientos, L. F., Battistelli, E. S., Battaglia, N., Bond, J. R., Brown, B., Burger, B., Calabrese, E., Chervenak, J., Crichton, D., Das, S., Devlin, M. J., Dicker, S. R., Bertrand Doriese, W., Dunkley, J., Dünner, R., Essinger-Hileman, T., Faber, D., Fisher, R. P., Fowler, J. W., Gallardo, P., Gordon, M. S., Gralla, M. B., Hajian, A., Halpern, M., Hasselfield, M., Hernández-Monteagudo, C., Hill, J. C., Hilton, G. C., Hilton, M., Hincks, A. D., Holtz, D., Huffenberger, K. M., Hughes, D. H., Hughes, J. P., Infante, L., Irwin, K. D., Jacobson, D. R., Johnstone, B., Baptiste Juin, J., Kaul, M., Klein, J., Kosowsky, A., Lau, J. M., Limon, M., Lin, Y.-T., Louis, T., Lupton, R. H., Marriage, T. A., Marsden, D., Martocci, K., Mauskopf, P., McLaren, M., Menanteau, F., Moodley, K., Moseley, H., Netterfield, C. B., Niemack, M. D., Page, L. A., Page, W. A., Parker, L., Partridge, B., Plimpton, R., Quintana, H., Reese, E. D., Reid, B., Rojas, F., Sehgal, N., Sherwin, B. D., Schmitt, B. L., Spergel, D. N., Staggs, S. T., Stryzak, O., Swetz, D. S., Switzer, E. R., Thornton, R., Trac, H., Tucker, C., Uehara, M., Visnjic, K., Warne, R., Wilson, G., Wollack, E., Zhao, Y., and Zunckel, C., "The Atacama Cosmology Telescope: cosmological parameters from three seasons of data," J. Cosmology Astropart. Phys. **10**, 60 (Oct. 2013). 1301.0824.

[7] Naess, S., Hasselfield, M., McMahon, J., Niemack, M. D., Addison, G. E., Ade, P. A. R., Allison, R., Amiri, M., Baker, A., Battaglia, N., Beall, J. A., de Bernardis, F., Bond, J., Britton, J., Calabrese, E., Cho, H.-m., Coughlin, K., Crichton, D., Das, S., Datta, R., Devlin, M. J., Dicker, S. R., Dunkley, J., Dünner, R., Fowler, J. W., Fox, A. E., Gallardo, P., Grace, E., Gralla, M., Hajian, A., Halpern, M., Henderson, S., Hill, J. C., Hilton, G. C., Hilton, M., Hincks, A. D., Hlozek, R., Ho, P., Hubmayr, J., Huffenberger, K. M., Hughes, J. P., Infante, L., Irwin, K., Jackson, R., Klein, J., Koopman, B., Kosowsky, A., Li, D., Louis, T., Lungu, M., Madhavacheril, M., Marriage, T. A., Maurin, L., Menanteau, F., Moodley, K., Munson, C., Newburgh, L., Nibarger, J., Nolta, M. R., Page, L. A., Pappas, C., Partridge, B., Rojas, F., Schmitt, B., Sehgal, N., Sherwin, B. D., Sievers, J., Simon, S., Spergel, D. N., Staggs, S. T., Switzer, E. R., Thornton, R., Trac, H., Tucker, C., Van Engelen, A., Ward, J., and Wollack, E. J., "The Atacama Cosmology Telescope: CMB Polarization at $200 < \ell < 9000$," *ArXiv e-prints* (May 2014). 1405.5524.

[8] Story, K. T., Reichardt, C. L., Hou, Z., Keisler, R., Aird, K. A., Benson, B. A., Bleem, L. E., Carlstrom, J. E., Chang, C. L., Cho, H.-M., Crawford, T. M., Crites, A. T., de Haan, T., Dobbs, M. A., Dudley, J., Follin, B., George, E. M., Halverson, N. W., Holder, G. P., Holzapfel, W. L., Hoover, S., Hrubes, J. D., Joy, M., Knox, L., Lee, A. T., Leitch, E. M., Lueker, M., Luong-Van, D., McMahon, J. J., Mehl, J., Meyer, S. S., Millea, M., Mohr, J. J., Montroy, T. E., Padin, S., Plagge, T., Pryke, C., Ruhl, J. E., Sayre, J. T., Schaffer, K. K., Shaw, L., Shirokoff, E., Spieler, H. G., Staniszewski, Z., Stark, A. A., van Engelen, A., Vanderlinde, K., Vieira, J. D., Williamson, R., and Zahn, O., "A Measurement of the Cosmic Microwave Background Damping Tail from the 2500-Square-Degree SPT-SZ Survey," ApJ **779**, 86 (Dec. 2013). 1210.7231.

[9] Anderson, L., Aubourg, E., Bailey, S., Bizyaev, D., Blanton, M., Bolton, A. S., Brinkmann, J., Brownstein, J. R., Burden, A., Cuesta, A. J., da Costa, L. A. N., Dawson, K. S., de Putter, R., Eisenstein, D. J., Gunn, J. E., Guo, H., Hamilton, J.-C., Harding, P., Ho, S., Honscheid, K., Kazin, E., Kirkby, D., Kneib, J.-P., Labatie, A., Loomis, C., Lupton, R. H., Malanushenko, E., Malanushenko, V., Mandelbaum, R., Manera, M., Maraston, C., McBride, C. K., Mehta, K. T., Mena, O., Montesano, F., Muna, D., Nichol, R. C., Nuza, S. E., Olmstead, M. D., Oravetz, D., Padmanabhan, N., Palanque-Delabrouille, N., Pan, K., Parejko, J.,

Pâris, I., Percival, W. J., Petitjean, P., Prada, F., Reid, B., Roe, N. A., Ross, A. J., Ross, N. P., Samushia, L., Sánchez, A. G., Schlegel, D. J., Schneider, D. P., Scóccola, C. G., Seo, H.-J., Sheldon, E. S., Simmons, A., Skibba, R. A., Strauss, M. A., Swanson, M. E. C., Thomas, D., Tinker, J. L., Tojeiro, R., Magaña, M. V., Verde, L., Wagner, C., Wake, D. A., Weaver, B. A., Weinberg, D. H., White, M., Xu, X., Yèche, C., Zehavi, I., and Zhao, G.-B., "The clustering of galaxies in the SDSS-III Baryon Oscillation Spectroscopic Survey: baryon acoustic oscillations in the Data Release 9 spectroscopic galaxy sample," MNRAS **427**, 3435–3467 (Dec. 2012). 1203.6594.

[10] Riess, A. G., Macri, L., Casertano, S., Lampeitl, H., Ferguson, H. C., Filippenko, A. V., Jha, S. W., Li, W., and Chornock, R., "A 3% Solution: Determination of the Hubble Constant with the Hubble Space Telescope and Wide Field Camera 3," ApJ **730**, 119 (Apr. 2011). 1103.2976.

[11] BICEP1 Collaboration, Aikin, R., Bischoff, C., Buder, I., Kovac, J. M., Su, M., Ade, P. A. R., Battle, J. O., Bierman, E. M., Bock, J. J., Chiang, H. C., Dowell, C. D., Duband, L., Filippini, J., Hivon, E. F., Holzapfel, W. L., Hristov, V. V., Jones, W. C., Kaufman, J. P., Keating, B. G., Kuo, C. L., Leitch, E. M., Mason, P. V., Matsumura, T., Nguyen, H. T., Ponthieu, N., Pryke, C., Richter, S., Sheehy, C., Kernasovskiy, S. S., Takahashi, Y. D., Tolan, J. E., and Yoon, K. W., "Degree-Scale CMB Polarization Measurements from Three Years of BICEP1 Data," *ArXiv e-prints* (Oct. 2013). 1310.1422.

[12] QUaD Collaboration, Brown, M. L., Ade, P., Bock, J., Bowden, M., Cahill, G., Castro, P. G., Church, S., Culverhouse, T., Friedman, R. B., Ganga, K., Gear, W. K., Gupta, S., Hinderks, J., Kovac, J., Lange, A. E., Leitch, E., Melhuish, S. J., Memari, Y., Murphy, J. A., Orlando, A., O'Sullivan, C., Piccirillo, L., Pryke, C., Rajguru, N., Rusholme, B., Schwarz, R., Taylor, A. N., Thompson, K. L., Turner, A. H., Wu, E. Y. S., and Zemcov, M., "Improved Measurements of the Temperature and Polarization of the Cosmic Microwave Background from QUaD," ApJ **705**, 978–999 (Nov. 2009). 0906.1003.

[13] Guth, A. H., Kaiser, D. I., and Nomura, Y., "Inflationary paradigm after Planck 2013," *ArXiv e-prints* (Dec. 2013). 1312.7619.

[14] Boyle, L. A., Steinhardt, P. J., and Turok, N., "Cosmic gravitational-wave background in a cyclic universe," Phys. Rev. D **69**, 127302 (June 2004). hep-th/0307170.

[15] Planck Collaboration, Ade, P. A. R., Aghanim, N., Armitage-Caplan, C., Arnaud, M., Ashdown, M., Atrio-Barandela, F., Aumont, J., Baccigalupi, C., Banday, A. J., and et al., "Planck 2013 results. XXII. Constraints on inflation," *ArXiv e-prints* (Mar. 2013). 1303.5082.

[16] Kaufman, J. P., Miller, N. J., Shimon, M., Barkats, D., Bischoff, C., Buder, I., Keating, B. G., Kovac, J. M., Ade, P. A. R., Aikin, R., Battle, J. O., Bierman, E. M., Bock, J. J., Chiang, H. C., Dowell, C. D., Duband, L., Filippini, J., Hivon, E. F., Holzapfel, W. L., Hristov, V. V., Jones, W. C., Kernasovskiy, S. S., Kuo, C. L., Leitch, E. M., Mason, P. V., Matsumura, T., Nguyen, H. T., Ponthieu, N., Pryke, C., Richter, S., Rocha, G., Sheehy, C., Su, M., Takahashi, Y. D., Tolan, J. E., and Yoon, K. W., "Self-Calibration of BICEP1 Three-Year Data and Constraints on Astrophysical Polarization Rotation," *ArXiv e-prints* (Dec. 2013). 1312.7877.

[17] Mortonson, M. J. and Seljak, U., "A joint analysis of Planck and BICEP2 B modes including dust polarization uncertainty," *ArXiv e-prints* (May 2014). 1405.5857.

[18] Flauger, R., Hill, J. C., and Spergel, D. N., "Toward an Understanding of Foreground Emission in the BICEP2 Region," *ArXiv e-prints* (May 2014). 1405.7351.

[19] O'Dea, D. T., Clark, C. N., Contaldi, C. R., and MacTavish, C. J., "A model for polarized microwave foreground emission from interstellar dust," MNRAS **419**, 1795–1803 (Jan. 2012). 1107.4612.

[20] Fraisse, A. A., Ade, P. A. R., Amiri, M., Benton, S. J., Bock, J. J., Bond, J. R., Bonetti, J. A., Bryan, S., Burger, B., Chiang, H. C., Clark, C. N., Contaldi, C. R., Crill, B. P., Davis, G., Doré, O., Farhang, M., Filippini, J. P., Fissel, L. M., Gandilo, N. N., Golwala, S., Gudmundsson, J. E., Hasselfield, M., Hilton, G., Holmes, W., Hristov, V. V., Irwin, K., Jones, W. C., Kuo, C. L., MacTavish, C. J., Mason, P. V., Montroy, T. E., Morford, T. A., Netterfield, C. B., O'Dea, D. T., Rahlin, A. S., Reintsema, C., Ruhl, J. E., Runyan, M. C., Schenker, M. A., Shariff, J. A., Soler, J. D., Trangsrud, A., Tucker, C., Tucker, R. S., Turner, A. D., and Wiebe, D., "SPIDER: probing the early Universe with a suborbital polarimeter," J. Cosmology Astropart. Phys. **4**, 47 (Apr. 2013). 1106.3087.

[21] Filippini, J. P., Ade, P. A. R., Amiri, M., Benton, S. J., Bihary, R., Bock, J. J., Bond, J. R., Bonetti, J. A., Bryan, S. A., Burger, B., Chiang, H. C., Contaldi, C. R., Crill, B. P., Doré, O., Farhang, M., Fissel, L. M., Gandilo, N. N., Golwala, S. R., Gudmundsson, J. E., Halpern, M., Hasselfield, M., Hilton, G., Holmes, W., Hristov, V. V., Irwin, K. D., Jones, W. C., Kuo, C. L., MacTavish, C. J., Mason, P. V., Montroy, T. E., Morford, T. A., Netterfield, C. B., O'Dea, D. T., Rahlin, A. S., Reintsema, C. D., Ruhl, J. E., Runyan, M. C., Schenker, M. A., Shariff, J. A., Soler, J. D., Trangsrud, A., Tucker, C., Tucker, R. S., and Turner, A. D., "SPIDER: a balloon-borne CMB polarimeter for large angular scales," in [*Millimeter, Submillimeter, and Far-Infrared Detectors and Instrumentation for Astronomy V*], *Society of Photo-Optical Instrumentation Engineers (SPIE) Conference Series* **7741** (July 2010). 1106.2158.

[22] Austermann, J. E., Aird, K. A., Beall, J. A., Becker, D., Bender, A., Benson, B. A., Bleem, L. E., Britton, J., Carlstrom, J. E., Chang, C. L., Chiang, H. C., Cho, H.-M., Crawford, T. M., Crites, A. T., Datesman, A., de Haan, T., Dobbs, M. A., George, E. M., Halverson, N. W., Harrington, N., Henning, J. W., Hilton, G. C., Holder, G. P., Holzapfel, W. L., Hoover, S., Huang, N., Hubmayr, J., Irwin, K. D., Keisler, R., Kennedy, J., Knox, L., Lee, A. T., Leitch, E., Li, D., Lueker, M., Marrone, D. P., McMahon, J. J., Mehl, J., Meyer, S. S., Montroy, T. E., Natoli, T., Nibarger, J. P., Niemack, M. D., Novosad, V., Padin, S., Pryke, C., Reichardt, C. L., Ruhl, J. E., Saliwanchik, B. R., Sayre, J. T., Schaffer, K. K., Shirokoff, E., Stark, A. A., Story, K., Vanderlinde, K., Vieira, J. D., Wang, G., Williamson, R., Yefremenko, V., Yoon, K. W., and Zahn, O., "SPTpol: an instrument for CMB polarization measurements with the South Pole Telescope," in [*Millimeter, Submillimeter, and Far-Infrared Detectors and Instrumentation for Astronomy VI*], *Society of Photo-Optical Instrumentation Engineers (SPIE) Conference Series* **8452** (Sept. 2012). 1210.4970.

[23] Planck Collaboration, Ade, P. A. R., Aghanim, N., Alves, M. I. R., Armitage-Caplan, C., Arnaud, M., Ashdown, M., Atrio-Barandela, F., Aumont, J., Aussel, H., and et al., "Planck 2013 results. I. Overview of products and scientific results," *ArXiv e-prints* (Mar. 2013). 1303.5062.

[24] Planck Collaboration, Ade, P. A. R., Alves, M. I. R., Aniano, G., Armitage-Caplan, C., Arnaud, M., Atrio-Barandela, F., Aumont, J., Baccigalupi, C., Banday, A. J., Barreiro, R. B., Battaner, E., Benabed, K., Benoit-Lévy, A., Bernard, J.-P., Bersanelli, M., Bielewicz, P., Bock, J. J., Bond, J. R., Borrill, J., Bouchet, F. R., Boulanger, F., Burigana, C., Cardoso, J.-F., Catalano, A., Chamballu, A., Chiang, H. C., Colombo, L. P. L., Combet, C., Couchot, F., Coulais, A., Crill, B. P., Curto, A., Cuttaia, F., Danese, L., Davies, R. D., Davis, R. J., de Bernardis, P., de Zotti, G., Delabrouille, J., Désert, F.-X., Dickinson, C., Diego, J. M., Donzelli, S., Doré, O., Douspis, M., Dunkley, J., Dupac, X., Enßlin, T. A., Eriksen, H. K., Falgarone, E., Fanciullo, L., Finelli, F., Forni, O., Frailis, M., Fraisse, A. A., Franceschi, E., Galeotta, S., Ganga, K., Ghosh, T., Giard, M., González-Nuevo, J., Górski, K. M., Gregorio, A., Gruppuso, A., Guillet, V., Hansen, F. K., Harrison, D. L., Helou, G., Hernández-Monteagudo, C., Hildebrandt, S. R., Hivon, E., Hobson, M., Holmes, W. A., Hornstrup, A., Jaffe, A. H., Jaffe, T. R., Jones, W. C., Keihänen, E., Keskitalo, R., Kisner, T. S., Kneissl, R., Knoche, J., Kunz, M., Kurki-Suonio, H., Lagache, G., Lamarre, J.-M., Lasenby, A., Lawrence, C. R., Leahy, J. P., Leonardi, R., Levrier, F., Liguori, M., Lilje, P. B., Linden-Vørnle, M., López-Caniego, M., Lubin, P. M., Macías-Pérez, J. F., Maffei, B., Magalhães, A. M., Maino, D., Mandolesi, N., Maris, M., Marshall, D. J., Martin, P. G., Martínez-González, E., Masi, S., Matarrese, S., Mazzotta, P., Melchiorri, A., Mendes, L., Mennella, A., Migliaccio, M., Miville-Deschênes, M.-A., Moneti, A., Montier, L., Morgante, G., Mortlock, D., Munshi, D., Murphy, J. A., Naselsky, P., Nati, F., Natoli, P., Netterfield, C. B., Noviello, F., Novikov, D., Novikov, I., Oppermann, N., Oxborrow, C. A., Pagano, L., Pajot, F., Paoletti, D., Pasian, F., Perdereau, O., Perotto, L., Perrotta, F., Piacentini, F., Pietrobon, D., Plaszczynski, S., Pointecouteau, E., Polenta, G., Popa, L., Pratt, G. W., Rachen, J. P., Reach, W. T., Reinecke, M., Remazeilles, M., Renault, C., Ricciardi, S., Riller, T., Ristorcelli, I., Rocha, G., Rosset, C., Roudier, G., Rubiño-Martín, J. A., Rusholme, B., Salerno, E., Sandri, M., Savini, G., Scott, D., Spencer, L. D., Stolyarov, V., Stompor, R., Sudiwala, R., Sutton, D., Suur-Uski, A.-S., Sygnet, J.-F., Tauber, J. A., Terenzi, L., Toffolatti, L., Tomasi, M., Tristram, M., Tucci, M., Valenziano, L., Valiviita, J., Van Tent, B., Vielva, P., Villa, F., Wandelt, B. D., Zacchei, A., and Zonca, A., "Planck intermediate results. XXII. Frequency dependence of thermal emission from Galactic dust in intensity and polarization," *ArXiv e-prints* (May 2014). 1405.0874.

[25] Runyan, M. C., Ade, P. A. R., Amiri, M., Benton, S., Bihary, R., Bock, J. J., Bond, J. R., Bonetti, J. A., Bryan, S. A., Chiang, H. C., Contaldi, C. R., Crill, B. P., Dore, O., O'Dea, D., Farhang, M., Filippini, J. P., Fissel, L., Gandilo, N., Golwala, S. R., Gudmundsson, J. E., Hasselfield, M., Halpern, M., Hilton,

G., Holmes, W., Hristov, V. V., Irwin, K. D., Jones, W. C., Kuo, C. L., MacTavish, C. J., Mason, P. V., Morford, T. A., Montroy, T. E., Netterfield, C. B., Rahlin, A. S., Reintsema, C. D., Ruhl, J. E., Schenker, M. A., Shariff, J., Soler, J. D., Trangsrud, A., Tucker, R. S., Tucker, C. E., and Turner, A., "Design and performance of the SPIDER instrument," in [*Millimeter, Submillimeter, and Far-Infrared Detectors and Instrumentation for Astronomy V*], *Society of Photo-Optical Instrumentation Engineers (SPIE) Conference Series* **7741** (July 2010). 1106.2173.

[26] Takahashi, Y. D., Ade, P. A. R., Barkats, D., Battle, J. O., Bierman, E. M., Bock, J. J., Chiang, H. C., Dowell, C. D., Duband, L., Hivon, E. F., Holzapfel, W. L., Hristov, V. V., Jones, W. C., Keating, B. G., Kovac, J. M., Kuo, C. L., Lange, A. E., Leitch, E. M., Mason, P. V., Matsumura, T., Nguyen, H. T., Ponthieu, N., Pryke, C., Richter, S., Rocha, G., and Yoon, K. W., "Characterization of the BICEP Telescope for High-precision Cosmic Microwave Background Polarimetry," ApJ **711**, 1141–1156 (Mar. 2010). 0906.4069.

[27] Bryan, S. A., Ade, P. A. R., Amiri, M., Benton, S., Bihary, R., Bock, J. J., Bond, J. R., Bonetti, J. A., Chiang, H. C., Contaldi, C. R., Crill, B. P., O'Dea, D., Dore, O., Farhang, M., Filippini, J. P., Fissel, L., Gandilo, N., Golwala, S., Gudmundsson, J. E., Hasselfield, M., Halpern, M., Helson, K. R., Hilton, G., Holmes, W., Hristov, V. V., Irwin, K. D., Jones, W. C., Kuo, C. L., MacTavish, C. J., Mason, P., Morford, T., Montroy, T. E., Netterfield, C. B., Rahlin, A. S., Reintsema, C. D., Riley, D., Ruhl, J. E., Runyan, M. C., Schenker, M. A., Shariff, J., Soler, J. D., Transrud, A., Tucker, R., Tucker, C., and Turner, A., "Modeling and characterization of the SPIDER half-wave plate," in [*Millimeter, Submillimeter, and Far-Infrared Detectors and Instrumentation for Astronomy V*], *Society of Photo-Optical Instrumentation Engineers (SPIE) Conference Series* **7741** (July 2010). 1006.3874.

[28] O'Brient, R. et al. (2014). in preparation.

[29] Battistelli, E. S., Amiri, M., Burger, B., Halpern, M., Knotek, S., Ellis, M., Gao, X., Kelly, D., Macintosh, M., Irwin, K., and Reintsema, C., "Functional Description of Read-out Electronics for Time-Domain Multiplexed Bolometers for Millimeter and Sub-millimeter Astronomy," *Journal of Low Temperature Physics* **151**, 908–914 (May 2008).

[30] Gudmundsson, J. E., Ade, P. A. R., Amiri, M., Benton, S. J., Bihary, R., Bock, J. J., Bond, J. R., Bonetti, J. A., Bryan, S. A., Burger, B., Chiang, H. C., Contaldi, C. R., Crill, B. P., Doré, O., Farhang, M., Filippini, J., Fissel, L. M., Gandilo, N. N., Golwala, S. R., Halpern, M., Hasselfield, M., Hilton, G., Holmes, W., Hristov, V. V., Irwin, K. D., Jones, W. C., Kuo, C. L., MacTavish, C. J., Mason, P. V., Montroy, T. E., Morford, T. A., Netterfield, C. B., O'Dea, D. T., Rahlin, A. S., Reintsema, C. D., Ruhl, J. E., Runyan, M. C., Schenker, M. A., Shariff, J. A., Soler, J. D., Trangsrud, A., Tucker, C., Tucker, R. S., and Turner, A. D., "Thermal architecture for the SPIDER flight cryostat," in [*Millimeter, Submillimeter, and Far-Infrared Detectors and Instrumentation for Astronomy V*], *Society of Photo-Optical Instrumentation Engineers (SPIE) Conference Series* **7741** (July 2010). 1106.2507.

[31] Tucker, C. E. and Ade, P. A. R., "Thermal filtering for large aperture cryogenic detector arrays," in [*Millimeter and Submillimeter Detectors and Instrumentation for Astronomy III*], *Society of Photo-Optical Instrumentation Engineers (SPIE) Conference Series* **6275** (July 2006).

[32] Ade, P. A. R., Pisano, G., Tucker, C., and Weaver, S., "A review of metal mesh filters," in [*Millimeter and Submillimeter Detectors and Instrumentation for Astronomy III*], *Society of Photo-Optical Instrumentation Engineers (SPIE) Conference Series* **6275** (July 2006).

[33] Benton, S. J., Ade, P. A. R., Amiri, M., Angilè, F. E., Bock, J. J., Bond, J. R., Bryan, S. A., Chiang, H. C., Contaldi, C. R., Crill, B. P., Devlin, M. J., Dober, B., Doré, O. P., Farhang, M., Filippini, J. P., Fissel, L. M., Fraisse, A. A., Fukui, Y., Galitzki, N., Gambrel, A. E., Gandilo, N. N., Golwala, S. R., Gudmundsson, J. E., Halpern, M., Hasselfield, M., Hilton, G. C., Holmes, W. A., Hristov, V. V., Irwin, K. D., Jones, W. C., Kermish, Z. D., Klein, J., Korotkov, A. L., MacTavish, C. J., Mason, P. V., Matthews, T. G., Megerian, K. G., Moncelsi, L., Morford, T. A., Mroczkowski, T. K., Nagy, J. M., Netterfield, C. B., Novak, G., Nutter, D., Pascale, E., Poidevin, F., Rahlin, A. S., Reintsema, C. D., Ruhl, J. E., Runyan, M. C., Savini, G., Scott, D., Shariff, J. A., Soler, J. D., Thomas, N. E., Trangsrud, A., Truch, M. D., Tucker, C. E., Tucker, G. S., Tucker, R. S., Turner, A. D., Ward-Thompson, D., Weber, A. C., Wiebe, D. V., and Young, E. Y., "BLASTbus electronics: general-purpose readout and control for balloon-borne experiments," in [*Ground-based and Airborne Telescopes V*], *Presented at the Society of Photo-Optical Instrumentation Engineers (SPIE) Conference* **9145** (June 2014).

[34] Soler, J. D., Ade, P. A. R., Amiri, M., Benton, S. J., Bock, J. J., Bond, J. R., Bonetti, J. A., Bryan, S. A., Chiang, H. C., Contaldi, C. R., Crill, B. P., Doré, O. P., Farhang, M., Filippini, J. P., Fissel, L. M., Fraisse, A. A., Gambrel, A. E., Gandilo, N. N., Gudmundsson, J. E., Halpern, M., Hasselfield, M., Hilton, G. C., Holmes, W. A., Hristov, V. V., Irwin, K. D., Jones, W. C., Kermish, Z. D., MacTavish, C. J., Mason, P. V., Megerian, K. G., Moncelsi, L., Montroy, T. E., Morford, T. A., Nagy, J. M., Netterfield, C. B., Reintsema, C. D., Ruhl, J. E., Runyan, M. C., Shariff, J. A., Trangsrud, A., Tucker, C. E., Tucker, R. S., Turner, A. D., Weber, A. C., W. D. V., and Young, E. Y., "Design and Construction of a Carbon Fibre Gondola for the SPIDER Balloon-borne Telescope," in [*Ground-based and Airborne Telescopes V*], *Presented at the Society of Photo-Optical Instrumentation Engineers (SPIE) Conference* **9145** (June 2014).

[35] Shariff, J. A., Ade, P. A. R., Amiri, M., Benton, S. J., Bock, J. J., Bond, J. R., Bonetti, J. A., Bryan, S. A., Chiang, H. C., Contaldi, C. R., Crill, B. P., Doré, O. P., Farhang, M., Filippini, J. P., Fissel, L. M., Fraisse, A. A., Gambrel, A. E., Gandilo, N. N., Golwala, S., Gudmundsson, J. E., Halpern, M., Hasselfield, M., Hilton, G. C., Holmes, W. A., Hristov, V. V., Irwin, K. D., Jones, W. C., Kermish, Z. D., MacTavish, C. J., Mason, P. V., Megerian, K. G., Moncelsi, L., Montroy, T. E., Morford, T. A., Nagy, J. M., Netterfield, C. B., Rahlin, A. S., Reintsema, C. D., Ruhl, J. E., Runyan, M. C., Soler, J. D., Trangsrud, A., Tucker, C. E., Tucker, R. S., Turner, A. D., Weber, A. C., Wiebe, D. V., and Young, E. Y., "Pointing control for the SPIDER balloon-borne telescope," in [*Ground-based and Airborne Telescopes V*], *Presented at the Society of Photo-Optical Instrumentation Engineers (SPIE) Conference* **9145** (June 2014).

[36] Gandilo, N. N., Ade, P. A. R., Amiri, M., Angilè, F. E., Benton, S. J., Bock, J. J., Bond, J. R., Bonetti, J. A., Bryan, S. A., Chiang, H. C., Contaldi, C. R., Crill, B. P., Devlin, M. J., Dober, B., Doré, O. P., Farhang, M., Filippini, J. P., Fissel, L. M., Fraisse, A. A., Fukui, Y., Galitzki, N., Gambrel, A. E., Gudmundsson, J. E., Halpern, M., Hasselfield, M., Hilton, G. C., Holmes, W. A., Hristov, V. V., Irwin, K. D., Jones, W. C., Kermish, Z. D., Klein, J., Korotkov, A. L., MacTavish, C. J., Mason, P. V., Matthews, T. G., Megerian, K. G., Moncelsi, L., Montroy, T. E., Morford, T. A., Mroczkowski, T. K., Nagy, J. M., Netterfield, C. B., Novak, G., Nutter, D., Pascale, E., Poidevin, F., Rahlin, A. S., Reintsema, C. D., Ruhl, J. E., Runyan, M. C., Savini, G., Scott, D., Shariff, J. A., Soler, J. D., Thomas, N. E., Trangsrud, A., Truch, M. D., Tucker, C. E., Tucker, G. S., Tucker, R. S., Turner, A. D., Ward-Thompson, D., Weber, A. C., Wiebe, D. V., and Young, E. Y., "Attitude determination for balloon-borne experiments," in [*Ground-based and Airborne Telescopes V*], *Presented at the Society of Photo-Optical Instrumentation Engineers (SPIE) Conference* **9145** (June 2014).

[37] Pascale, E., Ade, P. A. R., Bock, J. J., Chapin, E. L., Chung, J., Devlin, M. J., Dicker, S., Griffin, M., Gundersen, J. O., Halpern, M., Hargrave, P. C., Hughes, D. H., Klein, J., MacTavish, C. J., Marsden, G., Martin, P. G., Martin, T. G., Mauskopf, P., Netterfield, C. B., Olmi, L., Patanchon, G., Rex, M., Scott, D., Semisch, C., Thomas, N., Truch, M. D. P., Tucker, C., Tucker, G. S., Viero, M. P., and Wiebe, D. V., "The Balloon-borne Large Aperture Submillimeter Telescope: BLAST," ApJ **681**, 400–414 (July 2008). 0711.3465.

[38] Jones, W. C., Montroy, T. E., Crill, B. P., Contaldi, C. R., Kisner, T. S., Lange, A. E., MacTavish, C. J., Netterfield, C. B., and Ruhl, J. E., "Instrumental and analytic methods for bolometric polarimetry," A&A **470**, 771–785 (Aug. 2007). astro-ph/0606606.

[39] Bryan, S. A., Montroy, T. E., and Ruhl, J. E., "Modeling dielectric half-wave plates for cosmic microwave background polarimetry using a Mueller matrix formalism," Appl. Opt. **49**, 6313 (Nov. 2010). 1006.3359.

[40] Bryan, S., *Half-wave Plates for the Spider Cosmic Microwave Background Polarimeter*, PhD thesis, Case Western Reserve University (Feb. 2014). 1402.2591.

[41] Trangsrud, A. R., *The SPIDER CMB Polarimeter*, PhD thesis, California Institute of Technology (July 2011).

[42] DeLong, L. E., Symko, O. G., and Wheatley, J. C., "Continuously operating he-4 evaporation refrigerator," *Review of Scientific Instruments* **42**(1), 147–150 (1971).

[43] Gudmundsson, J. E. et al. (2014). in preparation.

[44] Bapat, S. L., Narayankhedkar, K. G., and Lukose, T. P., "Experimental investigations of multilayer insulation," *Cryogenics* **30**, 711–719 (1990).

[45] Tucker, R. S., *Characterization of Detectors and Instrument Systematics for the SPIDER CMB Polarimeter*, PhD thesis, California Institute of Technology (June 2014).

[46] Irwin, K. D. and Hilton, G. C., [*Transition-Edge Sensors*], 63 (2005).

[47] MacTavish, C. J., Ade, P. A. R., Battistelli, E. S., Benton, S., Bihary, R., Bock, J. J., Bond, J. R., Brevik, J., Bryan, S., Contaldi, C. R., Crill, B. P., Doré, O., Fissel, L., Golwala, S. R., Halpern, M., Hilton, G., Holmes, W., Hristov, V. V., Irwin, K., Jones, W. C., Kuo, C. L., Lange, A. E., Lawrie, C., Martin, T. G., Mason, P., Montroy, T. E., Netterfield, C. B., Riley, D., Ruhl, J. E., Runyan, M., Trangsrud, A., Tucker, C., Turner, A., Viero, M., and Wiebe, D., "Spider Optimization: Probing the Systematics of a Large-Scale B-Mode Experiment," ApJ **689**, 655–665 (Dec. 2008).

[48] O'Dea, D. T., Ade, P. A. R., Amiri, M., Benton, S. J., Bock, J. J., Bond, J. R., Bonetti, J. A., Bryan, S., Burger, B., Chiang, H. C., Clark, C. N., Contaldi, C. R., Crill, B. P., Davis, G., Doré, O., Farhang, M., Filippini, J. P., Fissel, L. M., Fraisse, A. A., Gandilo, N. N., Golwala, S., Gudmundsson, J. E., Hasselfield, M., Hilton, G., Holmes, W., Hristov, V. V., Irwin, K., Jones, W. C., Kuo, C. L., MacTavish, C. J., Mason, P. V., Montroy, T. E., Morford, T. A., Netterfield, C. B., Rahlin, A. S., Reintsema, C., Ruhl, J. E., Runyan, M. C., Schenker, M. A., Shariff, J. A., Soler, J. D., Trangsrud, A., Tucker, C., Tucker, R. S., Turner, A. D., and Wiebe, D., "SPIDER Optimization. II. Optical, Magnetic, and Foreground Effects," ApJ **738**, 63 (Sept. 2011). 1102.0559.

[49] BICEP2 Collaboration, Ade, P. A. R., Aikin, R. W., Amiri, M., Barkats, D., Benton, S. J., Bischoff, C. A., Bock, J. J., Brevik, J. A., Buder, I., Bullock, E., Davis, G., Dowell, C. D., Duband, L., Filippini, J. P., Fliescher, S., Golwala, S. R., Halpern, M., Hasselfield, M., Hildebrandt, S. R., Hilton, G. C., Hristov, V. V., Irwin, K. D., Karkare, K. S., Kaufman, J. P., Keating, B. G., Kernasovskiy, S. A., Kovac, J. M., Kuo, C. L., Leitch, E. M., Llombart, N., Lueker, M., Netterfield, C. B., Nguyen, H. T., O'Brient, R., Ogburn, IV, R. W., Orlando, A., Pryke, C., Reintsema, C. D., Richter, S., Schwarz, R., Sheehy, C. D., Staniszewski, Z. K., Story, K. T., Sudiwala, R. V., Teply, G. P., Tolan, J. E., Turner, A. D., Vieregg, A. G., Wilson, P., Wong, C. L., and Yoon, K. W., "BICEP2 II: Experiment and Three-Year Data Set," *ArXiv e-prints* (Mar. 2014). 1403.4302.

[50] Columbia Scientific Balloon Facility, *LDB Science Enclosures* (2010).

[51] Battistelli, E. S., Amiri, M., Burger, B., Devlin, M. J., Dicker, S. R., Doriese, W. B., Dünner, R., Fisher, R. P., Fowler, J. W., Halpern, M., Hasselfield, M., Hilton, G. C., Hincks, A. D., Irwin, K. D., Kaul, M., Klein, J., Knotek, S., Lau, J. M., Limon, M., Marriage, T. A., Niemack, M. D., Page, L., Reintsema, C. D., Staggs, S. T., Swetz, D. S., Switzer, E. R., Thornton, R. J., and Zhao, Y., "Automated SQUID tuning procedure for kilo-pixel arrays of TES bolometers on the Atacama Cosmology Telescope," in [*Millimeter and Submillimeter Detectors and Instrumentation for Astronomy IV*], *Society of Photo-Optical Instrumentation Engineers (SPIE) Conference Series* **7020** (Aug. 2008).